How frequent are close supermassive binary black holes in powerful jet sources?

Martin G. H. Krause [1,2]★ Stanislav S. Shabala [1] Martin J. Hardcastle [2]
Geoffrey V. Bicknell [3] Hans Böhringer,[4] Gayoung Chon,[4] Mohammad A. Nawaz,[5]
Marc Sarzi[2,6] and Alexander Y. Wagner[7]

[1]*School of Natural Sciences, Private Bag 37, University of Tasmania, Hobart, TAS 7001, Australia*
[2]*Centre for Astrophysics Research, School of Physics, Astronomy and Mathematics, University of Hertfordshire, College Lane, Hatfield, Hertfordshire AL10 9AB, UK*
[3]*Research School of Astronomy and Astrophysics, The Australian National University, ACT 2611, Australia*
[4]*Max-Planck-Institut für extraterrestrische Physik, Giessenbachstrasse, Garching D-85748, Germany*
[5]*Escola de Artes, Ciencias e Humanidades, Universidade de Sao Paulo, Rua Arlindo Bettio, 1000, Sao Paulo, SP 03828-000, Brazil*
[6]*Armagh Observatory and Planetarium, College Hill, Armagh BT61 9DG, UK*
[7]*Center for Computational Sciences, University of Tsukuba, 1-1-1 Tennodai, Tsukuba, Ibaraki 305-8577 Japan*

ABSTRACT

Supermassive black hole binaries may be detectable by an upcoming suite of gravitational wave experiments. Their binary nature can also be revealed by radio jets via a short-period precession driven by the orbital motion as well as the geodetic precession at typically longer periods. We have investigated Karl G. Jansky Very Large Array and Multi-Element Radio Linked Interferometer Network (MERLIN) radio maps of powerful jet sources for morphological evidence of geodetic precession. For perhaps the best-studied source, Cygnus A, we find strong evidence for geodetic precession. Projection effects can enhance precession features, for which we find indications in strongly projected sources. For a complete sample of 33 3CR radio sources, we find strong evidence for jet precession in 24 cases (73 per cent). The morphology of the radio maps suggests that the precession periods are of the order of 10^6–10^7 yr. We consider different explanations for the morphological features and conclude that geodetic precession is the best explanation. The frequently observed gradual jet angle changes in samples of powerful blazars can be explained by orbital motion. Both observations can be explained simultaneously by postulating that a high fraction of powerful radio sources have subparsec supermassive black hole binaries. We consider complementary evidence and discuss if any jetted supermassive black hole with some indication of precession could be detected as individual gravitational wave source in the near future. This appears unlikely, with the possible exception of M87.

Key words: black hole physics – gravitational waves – galaxies: jets – radio continuum: galaxies.

1 INTRODUCTION

Black holes with masses of millions to billions of solar masses reside in the centres of most galaxies (e.g. Magorrian et al. 1998; Häring & Rix 2004; Capuzzo-Dolcetta & Tosta e Melo 2017). The hierarchical growth of galaxies by merging therefore inevitably leads to binary systems of supermassive black holes (Begelman, Blandford & Rees 1980). Plausible cases of wide separations are known (e.g.

Komossa et al. 2003), evidence for supermassive black hole binaries at separations of a parsec and less is accumulating (Graham et al. 2015; Li et al. 2016; Bansal et al. 2017), and possible hints for actual black hole mergers have been suggested (Merritt & Ekers 2002; Chiaberge et al. 2017). Recently, a double radio nucleus with subparsec separation has been resolved with Very Long BaseLine Interferometry (VLBI; Kharb, Lal & Merritt 2017).

Thus, we may be able to extend the mass range of direct detection of black hole merging via gravitational waves (e.g. Abbott et al. 2016) to that of supermassive black holes. The lower mass end of the supermassive regime is expected to become accessible with the

Laser Interferometer Space Antenna (LISA, up to about 10^7 M$_\odot$, Amaro-Seoane et al. 2012), whereas the Square Kilometre Array pulsar timing array will be able to constrain the highest known black hole masses in the cosmic neighbourhood (e.g. Zhu et al. 2015).

Detailed simulations of the galaxy merging process with zoom simulations of the central parsec including post-Newtonian corrections predict that any contained black holes are driven to subparsec separations within 10^{7-8} yr, where they stay for another 10^{7-9} yr, these time-scales being shorter at higher redshift (Khan et al. 2016; Mayer 2017). The latter case can be probed with radio observations if at least one of the black holes is spinning and produces a jet.

If a jet-producing supermassive black hole is a member of a close binary system, one expects two observable effects (for a review Begelman et al. 1980; Begelman, Blandford & Rees 1984). First, the orbital motion imposes a widening helical pattern on the jet. For subparsec supermassive black hole binaries, orbital periods from less than a year to many thousands of years are expected, corresponding to structure on scales of parsecs up to about a kiloparsec. Secondly, both spin axes, likely coincident with the jet axes (Begelman et al. 1980; Merritt & Ekers 2002) precess around the orbital angular momentum vector due to the geodetic precession. The effect is caused by the motion of the masses, similar to the magnetic force being caused by the motion of electric charges. Massive black holes with subparsec separations can produce periods of the order of 10^6 yr, significantly less than the typical ages of observed radio sources, 10^7–10^8 yr (e.g. Krause 2005; English, Hardcastle & Krause 2016; Harwood et al. 2017; Turner, Shabala & Krause 2018), such that jet–lobe asymmetries and jet curvature would be visible on radio maps of 100 kpc scale jets.

Orbital motion and jet precession have been discussed and detections have been claimed for many individual jetted supermassive black hole systems. (e.g. Ekers et al. 1978; Gower & Hutchings 1982; Gower et al. 1982; Baryshev 1983; Hutchings, Price & Gower 1988; Abraham & Carrara 1998; Morganti et al. 1999b; Steenbrugge & Blundell 2008; Kharb et al. 2014; Kun et al. 2014, 2015; Ekers 2014; Britzen et al. 2017). Derived periods are indeed typically of the order of 10–1000 yr for VLBI and 10^5–10^7 yr for shorter baseline observations (VLA), as expected for parsec-scale supermassive black hole binaries and reflecting the sensitivity range given by the scale of the respective radio maps.

Here, we address the question of how common the evidence for binary black holes is among powerful extragalactic radio sources. We first investigate the object with probably the best available data on all spatial scales, Cygnus A, and show that both the 100 kpc scale and parsec-scale morphology shows evidence for perturbations of the jet consistent with a subparsec supermassive binary (Section 3.1). Because one prediction from relativistic aberration theory is that precession effects become more pronounced in more strongly projected sources, we investigate the two broad-line radio galaxies (BLRGs) with high-quality radio maps in the 2Jy sample in Section 3.2. They show clear evidence of precession, pointing to close binary supermassive black holes. In a complete sample of radio galaxies (derived from the 3CRR sample), we find morphological evidence for close binary supermassive black holes in 73 per cent of the sources (Section 3.3). In Section 4, we discuss our findings in the context of other work, in particular the possibility of direct detections of jetted supermassive binary black holes via gravitational waves (Section 4.5). We conclude in Section 5 that subparsec supermassive binary black holes appear to be a common feature for powerful jet sources, but will in general be challenging to detect with gravitational wave instruments.

2 DATA ANALYSIS

2.1 Radio maps and X-ray data

We use published radio maps throughout, except where otherwise stated. The 5 GHz VLA map of Cygnus A was previously published in Carilli & Barthel (1996).[1] We also used the VLBI maps from Boccardi et al. (2014, 2016a,b).[2] We used archival Chandra ACIS-I observations for Cyg A taken in VFAINT mode and performed standard data analysis with CIAO 4.8 with calibration data base (CALDB) 4.7.1. This includes flare cleaning by filtering light curves of source-free regions, VFAINT mode, gain, and charge transfer inefficiency corrections (Chon et al. 2012). The total cleaned exposure amounts to 3.2 Ms for the image presented in this paper. An ACIS blank sky observation was used for our background estimate after the normalization was adjusted. We used the 9–12.5 keV count rate to get the appropriate normalization for the background exposure.

We made use of the 2Jy sample (Wall & Peacock 1985) and associated data compilation.[3] The 5GHz data for 3C 17 and 3C 327.1 were downloaded from the VLA archive and reduced with standard data analysis methods (AIPS). The 3C 17 image uses archival data at A, B, and C configurations, and the 3C 327.1 one uses A and B configurations. The project IDs are AS179, AD419, AM548, and AM270.

We also analysed a complete sample (Black et al. 1992; Hardcastle et al. 1997, 1998; Leahy et al. 1997; Gilbert et al. 2004; Mullin, Hardcastle & Riley 2006; Mullin, Riley & Hardcastle 2008) of 98 radio galaxies based on the 3CRR catalogue (Laing, Riley & Longair 1983). The selection criteria were Fanaroff & Riley (1974, FR) class II (edge-brightened, powerful radio galaxies), redshift less than unity. Radio flux at 178 MHz >10.9 Jy, declination >10°, and Galactic latitude $|b| > 10°$ are inherited from the 3CRR sample. The data are available from: https://zl1.extragalactic.info. The radio maps have a resolution of typically 1 arcsec or better and have been obtained with the VLA and Multi-Element Radio Linked Interferometer Network (MERLIN) radio telescopes. We considered the sources where the data base shows at least one definite jet detection. Exceptions are 4C12.03, 3C 219, and 3C 341 where we decided after careful re-assessment of the original data that the previously identified jets are more likely thin lobes of a restarted radio source. Therefore, we did not consider these three sources. The final sample we used for the present study comprises 33 radio sources with high-quality radio maps for which jets had previously been identified. We show the radio maps in Appendix B.

2.2 Assessment of jet precession

To determine whether a jet is precessing or not, one needs to consider the intrinsic features of precessing jets as well as possible complications such as the jet–environment interaction.

2.2.1 Jet stability and deflections

In the simplest case, an FR II radio source inflates a lobe that is of comparable density with respect to the jet (e.g. Krause 2003;

---

[1] Kindly provided in electronic format by Chris Carilli and Rick Perley.
[2] We adopted the radio map from Boccardi et al. (2014) in Fig. 1 under the Creative Commons Attribution – Non Commercial Share Alike Licence.
[3] C. Tadhunter, R. Morganti, D. Dicken (2014), The 2Jy Sample: https://2jy.extragalactic.info/The_2Jy_Sample.html.

English et al. 2016). A relativistic, supermagnetosonic jet is then safe from disruption by instabilities (e.g. Appl 1996; Aloy et al. 1999; Rosen et al. 1999a; Perucho, Martí & Hanasz 2004; Perucho et al. 2010), at least as long as the jet is not too strongly magnetized (e.g. Appl 1996; O'Neill, Beckwith & Begelman 2012). Jets attain their asymptotic velocity already close to the core (e.g. Komissarov et al. 2007; Porth & Fendt 2010). In any case, magnetic acceleration, which requires a finite opening angle, will not work on kpc scales, where the jets are expected to be collimated (e.g. Krause et al. 2012b). Each piece of plasma in the jet will therefore to first order follow a ballistic trajectory at constant velocity. The projection onto the sky plane due to relativistic aberration has been studied for example by Gower et al. (1982).

Possible complications include deflection at dense clouds in the centre of the host galaxy. Jet–cloud interactions are strong when such sources are young and the host galaxy is gas-rich, as shown in 3D simulations (Gaibler et al. 2012; Wagner, Bicknell & Umemura 2012; Mukherjee et al. 2016). The lobe length asymmetry in some sources, e.g. Cygnus A, probably still witnesses this early phase (Gaibler, Khochfar & Krause 2011).

The simulations show, however, that the jet path is cleared when the jet has traversed the scale height of the host galaxy ($\lesssim$kpc). Therefore, in comparatively old FR II sources, like Cygnus A and the sample considered here, jet–cloud interactions are unlikely to be much of an issue: a realistic giant molecular cloud, comparable in size to the jet diameter (say, 100 pc) can reasonably be expected to be of the order of $\eta^{-1} > 10^5$ times denser than the jet (Choi, Wiita & Ryu 2007). For a jet with bulk velocity v_j, momentum flux conservation then determines its head advance speed to be approximately $v_j\sqrt{\eta}$ (e.g. Krause & Camenzind 2001). The jet would have overcome such a cloud in at most 10^5 yr, a small fraction of the source age of 100 kpc scale radio sources. Interstellar clouds move so slowly that they are being ablated as they move into the jet path. Further, such deflections would lead to bright radio hotspots close to the core, which generally are not seen in the maps we show here, in good agreement with the expectation that any clouds in the jet path have been cleared out in the early evolution of the sources.

2.2.2 Dynamical or asymmetric environments

Another effect that is important in this context is the motion of the host galaxy relative to the surrounding hot ambient gas, either because the host galaxy is not the central member of the group or cluster, or because the latter has had a recent merger with another galaxy cluster or substructure, which happens comparatively frequently (Chon & Böhringer 2017). Simulations of jets with crosswinds show that the jets may be bent and are found towards the windward side of the lobes (Balsara & Norman 1992). Such cases may be recognized, however, because one expects a plane-symmetric effect for both jets (compare, e.g. 3C 98, Fig. B6), as opposed to S-symmetry for precession (e.g. 3C 334, Fig. B22). The 3D simulations of precessing jets with crosswinds of Rodríguez-Martínez et al. (2006) show that the S-symmetry should still be observable in such cases.

If a hydrostatic galaxy halo has elliptical or triaxial symmetry and a non-precessing jet propagates in a direction that is not aligned with one of the symmetry axes of the halo we also expect an S-symmetric morphology, similar to the morphology of precessing jets. In a 3D simulation with such a set-up, Rossi et al. (2017) find that the lobes adjust to the ambient pressure profile whereas the jets remain straight. This indeed produces an S-symmetric appearance

(their fig. 9), comparable to what is expected from precession. This may confuse the interpretation of individual sources, particularly, when the precession is slow enough, so that the jets appear straight. However, for non-precessing jets in triaxial haloes we expect no strong dependence of the misalignment angle between jet direction and lobe axis on the viewing angle, because the jet direction should not be correlated with the axes of the dark matter halo. For a precessing jet, this misalignment angle will be much smaller for edge-on sources than for smaller inclination. In the extreme case, when the line of sight is within the precession cone, the angle between jet and lobe axis is unconstrained.

This issue can therefore be addressed by examining strongly projected sources like BLRGs. We investigate the BLRGs in the 2 Jy flux-limited sample in Section 3.2 finding outstanding misalignments between jets and lobes. In a statistical analysis, we confirm this trend, but with low significance. We also note that the X-ray isophotes in Cygnus A outside of the jet-influenced region suggest that the halo is approximately spherically symmetric (Smith et al. 2002). Massive elliptical galaxies, the typical hosts of powerful jets, tend to be round, slow rotators (e.g. Weijmans et al. 2014), which also suggests that the underlying gravitational potential may often have close to spherical symmetry. Overall, this suggests that precession is more important than triaxiality of the hydrostatic galaxy halo for powerful jets.

We conclude that for large-scale ($\gtrsim$10 kpc) FR II radio sources, stability and jet–environment interaction are reasonably well understood, so that it appears possible to pick up a precession signal in the radio maps.

2.2.3 Signatures of precessing jets

Three-dimensional hydrodynamics simulations of precessing jets have demonstrated the morphological features that are specific to precessing jets (e.g. Cox, Gull & Scheuer 1991; Monceau-Baroux et al. 2014; Donohoe & Smith 2016), especially, when compared to simulations of the interaction of non-precessing jets with their environment (e.g. Wagner & Bicknell 2011; English et al. 2016). Distinctive features of precessing jets include gradually curving jets with S-symmetry if both jets are detected. In general, the jet direction differs from the symmetry axis of the lobes. This is, because the jet fluid moves at much higher velocity than the lobe advances into the environment. Thus, even if the jet ejection direction changes very little during the time it takes a piece of jet to travel from the jet formation region to the tip of the lobe, this current direction will still be misaligned with the lobe axis, which records a much longer term average. The impact of the jet on the lobe boundary causes a high-pressure hotspot (e.g. English et al. 2016), which will advance the lobe boundary, most strongly in the current jet direction. For slowly precessing jets, this may lead to lobe extensions. Faster precession might carve out (partial) rings near the tip of the lobe.

Hydra A is to our knowledge the only precessing extragalactic radio source, for which a dedicated 3D hydrodynamics simulation study has been carried out. Nawaz et al. (2016) were able to reproduce the radio morphology of the source with high accuracy. With a precession period of 1 Myr, they achieved a close match between the simulated and the observed radio maps, whereas for periods of 5 Myr or longer, the jet became too straight (more details in Appendix A).

Relativistic aberration effects (Gower et al. 1982) may affect the intrinsic symmetry between jet and counterjet, i.e. precessing sources are not necessarily exactly S-symmetric.
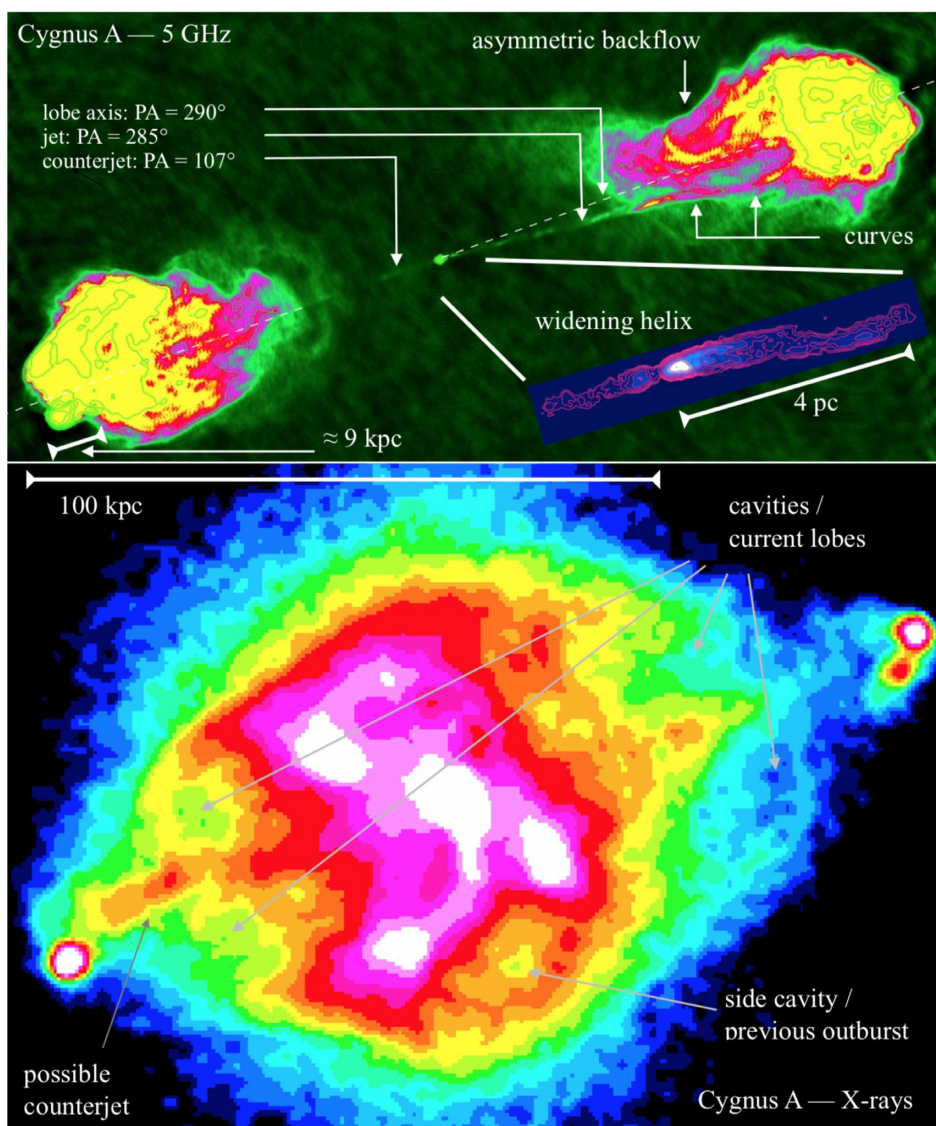
Figure 1. Cygnus A radio galaxy. Top: 5 GHz VLA image. Jet (right) and counterjet (left) are seen to emanate from the bright core in the middle of the image. The jet is directed towards position angle $PA = 285°$ and then curves first westwards and then north-west towards the hotspots. A fainter counterjet extends initially towards $PA = 107°$. The position angle of the jet in particular differs from the lobe axis. Credits: NRAO/AUI, Chris Carilli, and Rick Perley, Carilli & Barthel (1996). Inset: 43 GHz VLBI observation of the core region, showing helical motion in the parsec-scale jet (Boccardi et al. 2014). Bottom: *Chandra* X-ray colour map in the 0.5–2 keV band. Outer contours are close to spherically symmetric. Labelled: cavities coincides with the current radio lobes, a side cavity, possibly related to a previous outburst, a possible counterjet.

The criteria we used to assess the evidence for binary black holes for the presence of precession are as follows:

(C) – Jet curvature. A precessing jet curve and the shape of the jet depends on its precession parameters (precession angle, precession period). However, it is not straightforward to understand precession of jets from their observed curvature since the apparent jet structure strongly depends on the viewing direction. A precessing jet can appear with strong or mild curvature or even as a straight jet. The counterjet is usually more strongly curved than the approaching jet (relativistic aberration, compare Gower et al. 1982). While jet curvature may also be produced by temporal pressure imbalances or 3D instabilities, especially near the high-pressure hotspot (Hardee & Norman 1990), curvature is clearly a prime characteristic of a precessing jet (Scheuer 1982; Cox et al. 1991). We show in Appendix A that even for the comparatively weak jet source Hydra

A, a ballistic model for a precessing jet can reproduce the curvature in the jet well. Curved jets are particularly well visible in 3C 17, 3C 327.1 (Fig. 2), 3C 388 (Fig. B26), and 3C 401 (Fig. B28).

(E) – Jet at edge of lobe. In a precessing source the lobes conserve the long-term average jet direction (i.e. the orbital angular momentum direction for precessing jets from binary black holes), whereas the jet indicates the current direction of the jet-producing black hole's spin axis. The result can be visible as a jet at the lobe-edge, that is, a misalignment between the lobe axis and the jet direction will be introduced. Misalignment is well visible in Cygnus A (Fig. 1). Clear cases for jets at the edge of the lobe are, e.g. 3C 327.1 (Fig. 2) or 3C 334 (Fig. B22). Additionally, the back flow caused by a precessing jet is not isotropic. Therefore, a precessing jet will exhibit an asymmetry in lobe brightness, i.e. the lobe will be brighter in the side where the back flow is strong
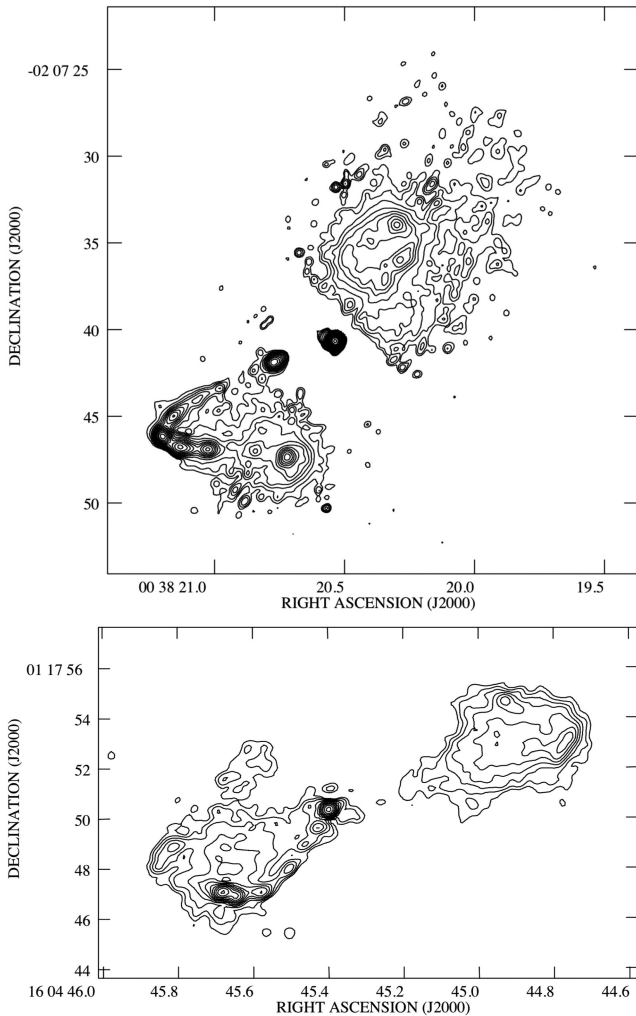
Figure 2. BLRGs 3C 17 (top) and 3C 327.1 (bottom) observed with the Very Large Array (Morganti et al. 1999a). Shown are 6 cm radio contours at $\sqrt{2}$ spacings.

and fainter on the other side. Cygnus A is an excellent example for this.

(R) – Wide/Multiple terminal hotspots possibly with ring-like features. A fast-precessing jet interacts with a wide area of environment at the jet-head location. As a result, multiple hotspots, wide hotspots, or a trail of hot back flow in a different direction than the jet may be visible. Sometimes any of the above features can appear as a shape of a ring or a partial ring. Such morphologies have been reproduced in detail in simulations (Williams & Gull 1985; Cox et al. 1991). Good examples for multiple hotspots include Cygnus A (Fig. 1) and 3C 20 (Fig. B1). A clear ring-like hotspot feature is seen in 3C 47 (Fig. B5).

(S) – S-symmetry of jets and hotspots. Jets/hotspots are found on opposite sides of a symmetry axis through the lobes. Good cases are 3C 200 (Fig. B10) and 3C 334 (Fig. B22).

For solid precession cases, we require that at least two precession characteristics are present. This accommodates the fact that there is a chance that factors such as interaction with a triaxial environment might also occasionally produce signatures comparable to the above. In particular, (C) and (E) can be produced by a crosswind, but unlikely in connection with S-symmetry, (S). Also, crosswinds are usually identifiable from the radio maps, and we indicate this

in the analysis below. We report curvature (C) in all sources, but make sure that a single occurrence of curvature does not bring a source with crosswind in the precessing jets category (the jet in 3C 382 curves twice in opposite directions). (R) appears unlikely to be caused by circumstances other than precession. (S) could in principal occur if a jet interacts with a triaxial halo, but we argued above that we expect this to be rare.

3 EVIDENCE FOR JET PRECESSION FROM KPC-SCALE JETS

An assessment of jet precession requires high-resolution radio maps of good quality. This is best available for powerful jet sources. We therefore first investigate what is perhaps the best-studied powerful radio source, Cygnus A. The 2 Jy sample and the complete sample of Mullin et al. (2008), which is derived from the 3CRR sample, contain powerful radio sources with excellent imaging data. The 2 Jy sample, however, has many southern sources without VLA coverage. We therefore use the 2 Jy sample for exemplifying the effects of projection and the complete sample of Mullin et al. (2008) for statistical results.

3.1 Cygnus A

The 5 GHz VLA radio map of Cygnus A, one of the best-studied extragalactic radio sources, is shown in Fig. 1. To first order, the source shows point reflection symmetry regarding the bright hotspots and the jets. The position angle of the jet differs by about 5° from the lobe axis (drawn here by eye). The backflow on the jet side at 5 GHz (highlighting relatively recently accelerated electrons) is clearly asymmetric with almost the entire backflow to the north of the jet. This is, however, a short-term feature, because the cavities in the *Chandra* X-ray map (Fig. 1, bottom) show that lobe plasma displaces X-ray gas also southwards of the jet. This is also confirmed in radio maps at lower frequency (Lazio et al. 2006; McKean et al. 2016). Both sides feature multiple hotspots in the 5 GHz map (see also Carilli et al. 1999). On the jet side, these are also observed in X-rays (for details Wilson, Young & Shopbell 2000). The western jet shows curvature. Cox et al. (1991) argue that in this case, the curvature likely results from interaction with an asymmetric backflow. We follow their analysis and conservatively do not assign the C-criterion to this source. The criteria E, R, and S we defined in Section 2.2.3 are satisfied.

The observed jet morphology cannot be explained by interaction with gas clumps, because the time-scale for ablation is too short, or hydrodynamic instabilities, as the jets are otherwise stable (compare Section 2.2.1). While on the scale of the radio lobes, the X-ray gas is strongly morphologically disturbed, the outer isophotes in the X-ray image (Fig. 1, bottom) are much more spherically symmetric. This has been shown rigorously by Smith et al. (2002). It is therefore very unlikely that interaction with an asymmetric environment is responsible for morphological features in this source (compare Section 2.2.2). X-ray and radio observations can therefore most naturally be explained by precession.

The precession period needs to be much shorter than the source age of about 24 Myr (Krause 2005), because otherwise we would not expect mirror symmetry in X-ray cavities and low-frequency radio maps, which is, however, observed (see above). This can also be seen when comparing to simulations of precessing jet sources. Donohoe & Smith (2016) present simulations of jets that reach a simulated age comparable to one precession cycle. For example, their fig. 14 shows a simulation after 1.5 precession cycles. Here,

the lobe shows strong asymmetries, which are not seen in Cygnus A (also compare the low-frequency images; Lazio et al. 2006; McKean et al. 2016). They find approximately symmetric lobes after about four precession cycles. For Cygnus A, we apply the lobe symmetry argument in the following way: in Fig. 1, the lobe has advanced further on the south side of the western jet, consistent with the current orientation of the jet. The eastern lobe has advanced further on the northern side of the jet. The difference is about 9 kpc. From the size and estimated age of the radio source, we estimate an average lobe advance speed of 3 kpc Myr^{-1} ($\approx$3000 km s^{-1}). From a comparison of ram pressure and hotspot pressure, Alexander & Pooley (1996) argue that the part where the jet currently impacts advances at roughly twice this speed. It would therefore take about 1.5 Myr to produce such an asymmetry via a precessing jet. Hence, if the precession period was longer than 3 Myr, the jet would remain on one side of the axis for too long and produce a much larger asymmetry. The precession period should therefore be less than 3 Myr. The jet is essentially straight through half of the lobe, i.e. for about 50 kpc. For a precessing jet to avoid showing observable curvature, the precession period needs to be much longer than the jet traveltime for the straight part of the jet. Because the jet is likely relativistic[4] (Krause 2005), this corresponds to the light traveltime, i.e. 0.15 Myr. We investigated precessing jet models using the model of Gower et al. (1982), varying precession period, jet phase, inclination, and precession cone opening angle. To reproduce a straight jet of comparable length to the one in Cygnus A, we needed a precession period of at least 0.5 Myr.

The morphological details shown in Fig. 1 therefore suggest a precession period of about 0.5–3 Myr.

3.2 Strongly projected radio sources

Strongly projected radio sources are of particular interest, because at low inclination, precessing jets have a high probability to be much more strongly misaligned with the lobe axis. In the extreme case that the line of sight is inside the precession cone, the jet can have any angle with respect to the lobe axis.

We first searched the 2 Jy sample of the brightest radio sources at 2.7 GHz for strongly projected sources. The data accessible from the sample web page show only poorly resolved quasars. Among the BLRGs, only 3C 17 and 3C 327.1 have high-quality radio maps with well-resolved jet as well as lobe detections (Fig. 2). Though the lobe axis is now much more difficult to determine, because of the strong contrast in brightness between the likely Doppler boosted jets and the fainter parts of the lobes, the misalignment is evident in both cases. We estimate misalignment angles of 21° for 3C 17 and 35° for 3C 327.1, much more than the 5° for Cygnus A.

---

[4]Estimating the Lorentz factor in the kpc-scale jet of Cygnus A is difficult (compare Carilli & Barthel 1996). One argument for a Lorentz factor of at least a few comes from a combination of hydrodynamics and radio luminosity. The ratio η between jet density and ambient density $\rho_{\mathrm{a}} = 0.05\rho_{\mathrm{a}*}m_{\mathrm{p}}$ cm^{-2}, with $\rho_{\mathrm{a}*} \approx 1$ (Smith et al. 2002), is $\eta = 10^{-4}\eta_*$, with $\eta_* \lesssim 1$, to explain hotspot advance speed and lobe width (Alexander & Pooley 1996; Rosen et al. 1999b; Krause 2005). The energy flux required to power the observed radio emission and to expand the radio source is $Q_0 = 2 \times 10^{46}Q_{0*}$ erg s^{-1}, with $Q_{0*} = 1$ (Kaiser & Alexander 1999). The jet radius is $r_{\mathrm{j}} = 0.55r_{\mathrm{j}*}$ kpc with $r_{\mathrm{j}*} \approx 1$(Carilli & Barthel 1996). Using the non-relativistic expression for the jet power then yields a jet velocity in units of the velocity of light of $\beta_{\mathrm{j}} = 8\,Q_{0*}^{1/3}r_{\mathrm{j}*}^{-2/3}\eta_*^{-1/3}\rho_{\mathrm{a}*}^{-1/3}$, which implies that the jet cannot be non-relativistic.

Both sources show curved jets with a sharp bend at the brightest jet knot (hotspot), suggesting that the jets may be deflected there before hitting the lobe boundary a second time at the final hotspot. It appears possible that the double hotspots in Cygnus A have a very similar origin.

The sources also have S-symmetry and the backflow on the jet side of 3C 327.1 is strongly asymmetric. These features are clear indicators for precession according to the criteria defined in Section 2.2.3. Because the length-scales are very similar to Cygnus A, the precession period must also be of the order of 10^6 yr.

There are 10 other BLRGs in the 2 Jy sample for which the data quality was not sufficient to assess the relative orientation of jet and lobe axis. 3C 17 and 3C 327.1 therefore only demonstrate that strong misalignment between jets and lobe axis may occur. We show statistics for the complete sample below.

3.3 A complete sample of powerful jet sources

To see if these are special cases, or if powerful radio sources commonly show similar evidence for jet precession, we have analysed the 33 high-resolution radio maps of a complete sample of powerful radio sources with redshifts less than one based on the 3CRR catalogue (Laing et al. 1983), only requiring a definite jet detection (for details, see Section 2.1). The jets in this sample have been identified previously, independently of the present analysis. We use the four criteria detailed in Section 2.2.3 to assess jet precession. Additionally, we assess the complexity of the source structure, e.g. if the source is affected by cross winds. If the source only shows features as expected for precessing jets (compare Section 2.2), we label it 'simple'. All radio maps are presented in Appendix B. The findings are summarized in Tables 1 and 2.

The most common features we find are jets at the edge of the lobe (24 occurrences) and ring-like/multiple/extended hotspots (23 occurrences). Jet curvature and S-symmetry are comparatively less important (14 and 11 occurrences, respectively, compare Table 2).

From our sample of 33 radio sources, we found no evidence for precession in four sources. Interestingly, three of these sources have a complex source morphology or crosswind, which complicated the assessment. In a further five sources, we found one of the above features per source. Since any one given feature might have different explanations, we regarded only sources with at least two independent indicators as solid precession cases. Of such sources, we have 24 in the sample, corresponding to a fraction of 73 per cent. 14 sources or 42 per cent show three or four features expected from precession, simultaneously. The high fraction of sources with multiple indicators of precession in our sample suggests that precession is very common among powerful radio sources.

We estimate the order of magnitude for the precession period for the sample in the following way: for jets to remain straight for tens of and sometimes over 100 kpc (compare Table 1), the precession period needs to be significantly longer than the light traveltime through the straight parts of the jets. This limits precession periods from below to be greater than or equal to about 0.5 to 5 Myr.

Where the lobes are well observed, the lobe near where the jet impacts (hotspot) is not further advanced than other parts, see for example 3C 33.1, 3C 41, 3C 47, 3C 200 (north), 4C 74.16 (south). Multiple hotspots, where the jet interacts with the lobe boundary, or ring-like hotspots imply that the jet interacts with the lobe boundary for a time that is short compared to the source age. Otherwise the lobe boundary (a sharp rise in density) would be deformed. These

Table 1. Evidence for binary black holes in a complete sample of powerful jet sources derived from the 3CRR catalogue. Columns from left to right: Optical type (see Section 2.1 for the data base webpage): NLRG: narrow-line radio galaxy, BLRG: broad-line radio galaxy, LERG: Low excitation radio galaxy, Q: quasar. Structure: x-wind for crosswind. Precession: letters refer to precession criteria defined in Section 2.2.3. Misalignment: angle between jet and lobe axis, if lobes are detected and a lobe axis can be assigned. Source size corresponds to data base entry 'sum of linear lobe lengths'. Jet length corresponds to data base entry 'straight jet length'. Age is the model age from Turner et al. (2018), where available.

Source	Opt. t.	Struct.	Prec.	Misalign.	Source size (kpc)	Straight jet (kpc)	Age (log, yr)
3C 20	NLRG	simple/x-wind	CERS	–	139	37	–
3C 22	BLRG	simple	ES	–	206	83	7.1 ± 0.2
3C 33.1	BLRG	simple	CES	0°	691	156	8.4 ± 0.2
3C 41	NLRG	simple	CERS	5°	180	61	–
3C 47	Q	simple	ERS	6°	325	166	7.8 ± 0.2
3C 98	NLRG	simple/x-wind	C	0°	169	62	8.8 ± 0.4
3C 171	NLRG	complex	CER	–	37	12	–
3C 173.1	LERG	simple	R	–	248	49	7.7 ± 0.2
3C 175	Q	simple	R	–	374	150	7.4 ± 0.2
3C 200	NLRG	simple	CERS	12°	144	41	7.3 ± 0.3
3C 207	Q	complex	ER	–	88	35	–
3C 220.1	NLRG	simple	CER	0°	216	79	–
3C 228	NLRG	simple	–	0°	300	45	7.3 ± 0.2
3C 234	NLRG	complex	–	–	295	183	8.3 ± 0.2
4C 74.16	NLRG	simple	ER	6°	312	76	–
3C 249.1	Q	complex	–	–	119	21	7.7 ± 0.2
3C 263	Q	complex	E	–	341	16	–
3C 275.1	Q	simple	CE	–	118	53	–
3C 285	LERG	complex/x-wind	E	–	260	72	8.9 ± 0.3
3C 300	NLRG	simple	ER	–	394	20	–
3C 303	BLRG	complex	ER	41°	107	31	8.4 ± 0.3
3C 334	Q	simple	CERS	22°	326	83	–
3C 336	Q	simple	ERS	–	201	38	7.2 ± 0.2
3C 352	NLRG	simple	ER	10°	96	29	–
3C 382	BLRG	simple/x-wind	CR	0°	190	54	–
3C 388	LERG	simple	CR	0°	72	14	–
3C 390.3	BLRG	simple/x-wind	ER	4°	243	98	–
3C 401	LERG	simple	CER	0°	79	19	–
3C 433	NLRG	complex	CER	–	105	8	–
3C 436	NLRG	simple	ERS	2°	368	70	7.9 ± 0.2
3C 438	LERG	simple	CERS	4°, 12°	94	38	–
3C 441	NLRG	simple	ERS	–	256	62	–
3C 452	NLRG	simple/x-wind	–	0°	417	71	8.5 ± 0.2

Table 2. Statistics of Table 1.

Criterion	Occurrence
Curvature (C)	14
Jet towards Edge of Lobe (E)	24
Ring/multiple/extended hotspot (R)	23
S-symmetry (S)	11

features have been confirmed in simulations of precessing jets by Cox et al. (1991). Clear symmetric ring features are seen in 3C 47, 3C 388, and 3C 441 (south). Double hotspots that could arise from interaction with a roughly symmetric lobe boundary are seen in, e.g. 3C 20. A hotspot on one side of the lobe with a bright extension outlining a symmetric lobe boundary near the tip of the lobe is seen in 3C 200, 4C 74.16, and 3C 334. The ages for some of our sources have been modelled by Turner et al. (2018) and are included in Table 1. They are in the range 10^7–10^9 yr. The sizes of the sources that have no age estimates are similar (Table 1). Therefore, their ages are most likely also similar. These morphological features suggest precession periods of about a tenth of the source ages or less, i.e. a few to a few tens of Myr.

In summary, morphological analysis of jets and lobes suggests precession periods of the order of 1–10 Myr, in any case significantly less than the source age.

We note that mild curvature is seen in about half of the precessing sources. While this can also be the result of hydrodynamic processes in the lobe (one reason why we require at least two precession criteria above), it would be expected if the precession period was of the order of 1–10 Myr, as found above. Literature estimates for the precession period for the precessing sources in our sample include 0.5 Myr for 3C 388 (from fitting a relativistic, precessing jet model; Gower et al. 1982) and >3 Myr for 3C 390.3 (flow model from spectral analysis; Alexander 1985).

We also repeated the test for orientation dependence of the jet–lobe axis misalignment in this sample of powerful radio sources based on the 3CRR catalogue. As expected, it is more difficult to assess the shape of the radio lobes in the more strongly projected sources due to a combination of beaming effects and limited dynamic range of the images. We were able to estimate the misalignment angle in 2 of the 8 quasars, 4 of the 5 BLRGs, 9 of the 15 narrow line radio galaxies (NLRGs), and 3 of the 5 low excitation radio galaxies (LERGs). The largest misalignment angle for

NLRGs is 12° whereas among BLRGs and quasars values of up to 41° are found. Low values are observed in both groups. Mean and standard deviation of the two distributions are $4° \pm 4°$ for the NLRGs and $12° \pm 15°$ for BLRGs and quasars. The p-value for the Kolmogorov–Smirnov test, i.e. the probability that both distributions are from the same parent sample, is 72 per cent. At the current sample size, there is therefore no significant difference between the two distributions. However, there is an indication that the misalignment in BLRGs and quasars is stronger, as expected, if precession was a significant factor.

4 DISCUSSION: THE CASE FOR CLOSE BINARY BLACK HOLES

Subparsec supermassive black hole binaries with jets may produce observable effects on the 100 kpc scale via geodetic precession, and at the same time show morphological features on parsec scale due to their orbital motion. Due to observational limitations, both effects will rarely be observable in the same source: lobe structure is best studied in radio galaxies where the jet has a large angle to the line of sight, whereas well-observed parsec-scale jets are usually strongly Doppler boosted, with small inclinations and thus have poor lobe images due to limited dynamic range. To make the case, we present a rare example with very good observations on parsec as well as 100 kpc scales, Cygnus A, and search for evidence of, respectively, orbital and geodetic precession separately in samples of 100 kpc scale radio galaxies (Section 3) and parsec-scale radio sources from the literature (Section 4.3 below). We first discuss if the precession observed in 100 kpc scale radio sources could be a consequence of geodetic precession. Based on this likely being the case, we then make the case for a supermassive binary black hole in Cygnus A, where we argue that geodetic and orbital precession are seen. We then discuss evidence for orbital precession in parsec-scale, powerful radio sources. Finally, we investigate if any supermassive binary black hole candidate inferred from precession in extragalactic radio sources could be confirmed via an individual gravitational wave detection in the near future.

4.1 Causes of precession in 100 kpc scale radio sources

Jet formation models and explanations of differing radio-loudness of quasars are often based on the assumption that jets, in particular powerful ones as studied here are produced by fast-spinning black holes (e.g. Moderski, Sikora & Lasota 1998; Koide et al. 2000; De Villiers, Hawley & Krolik 2003; Komissarov & McKinney 2007; Beckwith, Hawley & Krolik 2008; Ghisellini et al. 2014; Gardner & Done 2018), even though direct evidence for this is so far elusive (Fender, Gallo & Russell 2010). In such models, the instantaneous jet direction is given by the spin axis. Hence, it is likely that changes in jet direction are caused by corresponding changes of the spin axis of the jet-producing black hole (compare also Begelman et al. 1980, 1984; Merritt & Ekers 2002). Known mechanisms that may affect the jet direction include orbital motion and geodetic precession in a black hole binary, and interaction with the angular momentum of a disc around the black hole, which may be the accretion disc.

4.1.1 Geodetic precession

A natural explanation for precession of jets is via the geodetic precession of the black hole spins in a binary system where the jet is ejected along the spin axis of one of the black holes. The geodetic precession period in Myr, $P_{gp, Myr}$, for binary black holes with total mass $M_9 10^9$ M$_\odot$, mass ratio r and separation of d_{pc} pc in a circular orbit is given by (Barker & O'Connell 1975; Stairs 2003; Thorne & Blandford 2017)

$$P_{gp,Myr} = 124 \frac{(1+r)^2}{r(3r+4)} d_{pc}^{5/2} M_9^{-3/2}. \tag{1}$$

For powerful jets, it is reasonable to assume that the observed jet is produced by the more massive black hole. Therefore, the mass ratio cannot exceed unity. Equation (1) can then be written as an upper limit for the binary separation:

$$d_{pc} < 0.18 \, P_{gp,Myr}^{2/5} M_9^{3/5}. \tag{2}$$

We have argued above that VLA radio maps of powerful jet sources suggest that precession periods of the order of Myr are very common. Many of these sources (e.g. Cygnus A, Tadhunter et al. 2003) are known from independent analyses to have central dark masses of the order of 10^9 M$_\odot$. Masses of supermassive black holes in general extend up to about 10^{10} M$_\odot$ (e.g. Häring & Rix 2004; Peterson et al. 2004; Gebhardt et al. 2011; Bogdán et al. 2018). It is therefore clear that a measurement of precession periods of the order of Myr implies subparsec supermassive black hole binaries, if the precession is caused by this mechanism.

4.1.2 Other precession mechanisms

It is difficult to explain a sustained precession with a period of the order of Myr with other mechanisms.

If the precession period of the order of Myr we argued for above corresponded to an orbital period, the separation of the binary would be $48 M_9^{1/3}$ pc and the Keplerian velocity $298 M_9^{1/3}$ km s^{-1}. For a jet at a velocity comparable to the speed of light, this would lead to a precession cone opening angle of less than a degree. This would be far too small to be observable and inconsistent with the jet–lobe axis misalignments in our observations.

Torques caused by a misalignment between the spin axis of a black hole and the angular momentum of the accretion disc can also induce jet precession. In an overall misaligned system the inner part of the accretion disc is aligned with the black hole spin axis by the combined effect of Lense–Thirring precession and internal viscosity of the disc. This process is known as the Bardeen–Petterson effect (Bardeen & Petterson 1975). The outer disc will maintain its angular momentum direction. Through the accretion of material of the outer disc on to the black hole, the black hole spin axis will precess and align with the outer disc. The precession time-scale is of the same order as the alignment time-scale (Scheuer & Feiler 1996). Two aspects of the disc-induced precession, namely the relatively slow precession rate and the single possible precession cycle in the alignment lifetime (Scheuer & Feiler 1996; Lodato & Pringle 2006), make this process less likely to be a cause of jet precession for the given radio sources. For example, following Lodato & Pringle (2006), adopting their numerical values for accretion efficiency ε and disc viscosity parameters $\alpha_{1,2}$ and assuming black hole spin $a \approx 1$, we obtain a precession period of

$$t_{prec} \approx t_{align} \approx 7 \text{ Myr}$$
$$\times a^{11/16} \left(\frac{\epsilon}{0.1}\right)^{7/8} \left(\frac{L}{0.1 L_{Edd}}\right)^{-7/8} M_9^{-1/16} \tag{3}$$
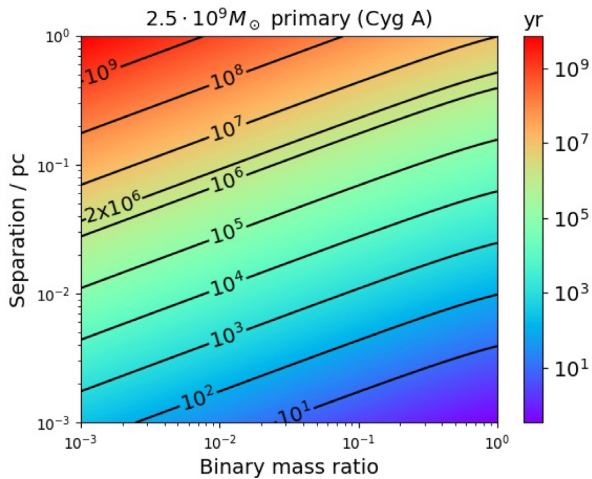$$\times \left(\frac{\alpha_1}{0.03}\right)^{15/16} \left(\frac{\alpha_2}{0.3}\right)^{-11/16}.$$

Figure 3. Graphical representation of the geodetic precession period for Cygnus A as a function of mass ratio and binary separation. A precession period of 1–2 Myr, as estimated from the VLA image requires a binary separation less than 0.4 pc.

This is larger than the precession period we estimated for Cygnus A. Simulations show that if the precession time-scale becomes comparable to the source age, very asymmetric lobe morphologies result (Donohoe & Smith 2016). As discussed in Section 3.3, the sources in our sample do not show such asymmetries, but often show smooth, ring-like hotspot features that suggest a local impact time-scale short compared to the source ages and thus many precession cycles. This is not consistent with precession induced by a misaligned accretion disc. A process that produces one precession cycle only, where the period of the cycle can be much shorter than the source age (equation 3), would have only a limited probability to be detected at the time a given source is observed. However, we also find precession frequently in comparatively old sources, e.g. 3C 33.1, 3C 303, and 3C 436. These are three of the seven sources with modelled ages of log(age/yr) ≥ 7.9. This makes disc-induced precession less likely for this subpopulation.

A pancake like, dense nuclear star cluster could also cause a precession to a misaligned black hole spin (Appl, Sol & Vicente 1996b). The induced precession period is, however, of the order of 10^9 yr or longer for plausible parameters of nuclear star clusters, and hence not of interest in the present context.

4.2 The case for a supermassive black hole binary in Cygnus A

For Cygnus A, where $M_9 = 2.5$ (Tadhunter et al. 2003), a precession period of 0.5–3 Myr would imply a separation < 0.5 pc (compare Fig. 3). Fig. 1 also shows the 43 GHz VLBI image of the centre of Cygnus A (Boccardi et al. 2014, 2016a). The structure of the jet shows a helical pattern with a wavelength of roughly $\lambda = 4$ pc. If this is caused by a jet from a binary black hole, the implied Keplerian orbital period is $P_{orb} = \lambda/v_j \approx 18$ yr, where we have used a jet velocity of $v_j = 0.7c$ consistent with multi-epoch observations (Boccardi et al. 2016a). This implies a binary separation of 0.05 pc.

In order to investigate this scenario further, we can look at the implied constraint on the mass ratio: the combination of total mass, precession period and a binary separation of 0.05 pc determine the mass ratio uniquely as $r \lesssim 10^{-2}$ (compare Fig. 3). Such significant differences in mass are expected from cosmological evolution: black hole mass scales with galaxy bulge mass (Häring & Rix 2004), and

since minor galaxy mergers occur much more frequently than major ones, very different masses should be the rule (Rodriguez-Gomez et al. 2015).

If the mass ratio were indeed $r \lesssim 10^{-2}$, orbital motion alone could only produce a helical jet in the secondary, because the centre of mass would be much closer to the primary, such that its orbital velocity would be small, resulting in a too narrow a precession cone. Because the high power of the main radio source requires a jet from the bigger black hole (Krause 2005), this would support the conclusion that both black holes are currently producing a jet: the bigger one would be responsible for the main radio structure, the smaller one would significantly contribute to the emission on the parsec scale, so that the helical morphology could be produced. This would, however, not be expected, as one would expect the mass ratio (1:100) to be reflected in the ratio of jet luminosities.

In an alternative model with two black holes of similar masses and only one jet the separation would have to be about 0.5 pc. Hence, the orbital period would be of the order of 1000 yr, corresponding to a predicted wavelength for the helical pattern of about 300 pc. This could therefore not explain the parsec-scale helical structure.

The model suggested by Lobanov & Roland (2005) for 3C 345 could also apply to Cygnus A. In this case, the presence of the secondary induces a precession of the accretion disc of the primary which causes the jet, ejected from the accretion disc around the primary, to precess.

Finally, an alternative method to estimate the binary separation is via the opening angle of the helical pattern. The half opening angle α is given by $\tan \alpha = v_o/v_j$. Since the orbital velocity v_o is related to the Keplerian orbital period P_K via $v_o = \pi d/P_K$, and the jet velocity $v_j = \lambda/P_K$, we can give the binary separation as function of the observables: $d = \lambda \tan \alpha/\pi$. Using $\alpha = 5°$ (Boccardi et al. 2016a), we find $d = 0.1$ pc, which supports the $r \approx 10^{-2}$ solution. Because of the observed complexity of the flow structure and absorption likely playing a role we regard this as a less accurate estimate.

The VLBI assessment of the mass ratio is therefore inconclusive, but more evidence seems to support a separation of 0.05–0.1 pc combined with a mass ratio of about 1:100.

The radio structures produced by the jets in Cygnus A have displaced the X-ray gas in certain regions (Fig. 1). The X-ray image reveals not only cavities produced by the current jet, but also at least one side cavity which is difficult to relate to the current jet activity or previous jets with the same orientation. Comparing to dedicated 3D simulations, we found that the side cavity is well explained by a preceding activity period where a jet was oriented at an angle of roughly 90° (Chon et al. 2012). This could be interpreted in the context of black hole mergers (Merritt & Ekers 2002), which would imply an additional supermassive black hole that has now merged. However, as shown above, a pause in jet activity for 10 Myr, but with strong accretion could have re-oriented the jet to the current position without the need of an additional black hole.

Precession models for Cygnus A have been presented before: Baryshev (1983) based the analysis on a radio map that was not sensitive enough to show the jets. Steenbrugge & Blundell (2008) have aligned the axis of the precession cone with the current jet direction, and fitted a ballistic jet path to the curvature highlighted in Fig. 1. 3D hydrodynamic modelling favours, however, the explanation that these jet curves are the result of interaction of the jet with the asymmetric backflow (Cox et al. 1991). Also, their precession model does not explain the misalignment of the jet with the lobe axis. In contrast, we interpret the overall jet–lobe axis misalignment as due to precession, and compare to BLRGs and a complete sample. In view of these new results, it appears possible that some of the jet

structure interpreted as due to precession in those previous models are actually due to unrelated local brightness variations. However, the precession period inferred from the previous modelling is even shorter than ours, which would re-enforce the case for a subparsec binary black hole in Cygnus A.

The recent discovery of a further supermassive black hole candidate in Cygnus A (Cyg A-2 Perley et al. 2017; Dabbech et al. 2018) cannot be related to the precession signatures discussed before. Cyg A-2 is located 460 pc away from the primary AGN (Cyg A-1) in projection, too far away to cause a detectable geodetic precession. The time-scale for a supermassive black hole with a mass of $m_8 10^8$ M$_\odot$ at the location of Cyg A-2 to approach Cyg A-1 to within a parsec is determined by dynamical friction, and is of the order of $10^7 m_8^{-1}$ yr (further depending on galaxy properties, e.g. Begelman et al. 1980). The time-scale for gravitational inspiral and coalescence for a supermassive black hole binary is $10^8 r^{-1}(M_9/2.5)^{-3}(d_{pc}/0.05)^4$ yr (Begelman et al. 1980). Both time-scales are highly uncertain. One might argue that the discovery of Cyg A-2 makes it less likely that there could be a further supermassive black hole in the system. However, a rate of several 10 Gyr^{-1} for 100:1 galaxy mergers would be consistent with the expectations from cosmological simulations for a massive galaxy like Cygnus A (Rodriguez-Gomez et al. 2015).

4.3 Orbital precession in parsec-scale jet sources

The orbital period P_{orb} of a black hole binary can be related to the geodetic precession period as

$$P_{orb} = 164 \text{ yr } P_{gp,Myr}^{3/5} \left[\frac{(1+r)^2}{r(3r+4)} \right]^{-3/5} M_9^{-7/5} . \quad (4)$$

This implies orbital time-scales of the order of 10–1000 yr for geodetic precession periods of the order of Myr and black hole masses of the order of 10^9 $M_\odot$ as argued for in the sample of powerful jet sources above. This should result in observable jet angle swings on the parsec scale, observable with VLBI, at least in sources where the jet comes from the smaller, secondary black hole, particularly, where the jet axis is close to the line of sight (blazars). Swings of the jet angle in parsec-scale radio jets have been frequently reported, e.g. 3C 273 (Savolainen et al. 2006), 3C 279 (Jorstad et al. 2004), or 3C 345 (Lobanov & Roland 2005). In the latter case, a subparsec black hole binary was suggested as the cause.

From monitoring an overall sample of 259 blazar jets, Lister et al. (2013) conclude that jet angle variations are very frequent.[5] In a subsample of the 60 most heavily observed blazar jets, they find potentially periodic reorientation of the jet in 12 sources where the periods would be 5–12 yr (the time base is not long enough yet for a firm detection of periodicity), 5 more with a back-and-forth trend, 14 others with a monotonic trend, and 29 with irregular changes. No source showed a constant jet angle. The sample was selected against obvious jet bends in the innermost jet structure. Thus, while the timebase is not long enough for a firm detection of periodicity, the observed variations in the jet angles are consistent with the expectations for binary black holes with orbital periods of

[5]Lister (2016) discuss whether the whole jets are precessing or only an energized section of a wider, conical flow. They argue that the latter might be more likely, because a precession of the whole jet would require enormous torques. Subparsec scale binary black holes, as suggested here, would, however, be able to provide such torques. Therefore, precession of the entire jet is a viable interpretation of the data.

10–1000 yr as suggested from our analysis of the 100 kpc scale, powerful jets.

From these 60 best observed sources, the majority were quasars (41 sources). Quasars are intrinsically more powerful than the weaker BL Lac objects, which constitute most of the rest of the sample, and are thus comparable to our powerful jet sources. Lister et al. (2013) show that for the quasars, the jet angle varies even more than for the BL Lac objects. These findings are in excellent agreement with the expectation, if powerful radio sources frequently had close binary black holes, as suggested already by Lobanov & Roland (2005) in the case of 3C 345.

4.4 Complementary evidence for the case of close binary black holes associated with powerful jet sources

Small-scale and large-scale jets are frequently misaligned with a secondary peak in the distribution function at 90°, possibly related to binaries (Appl, Sol & Vicente 1996a; Appl et al. 1996b; Kharb, Lister & Cooper 2010). Abrupt changes of ejection direction are known, as expected if jets are produced alternately by one or the other black hole of a binary with misaligned spins (Lister et al. 2013; Lu et al. 2013). Binaries with orbital periods of the order of 10 yr are also suggested by Gamma ray light curves of blazars, where the luminosity changes due to the relativistic Doppler boosting (Rieger 2007).

While X-shaped radio sources probably include examples that originate from peculiar jet–environment interactions (e.g. Kraft et al. 2005; Rossi et al. 2017), some may be related to binary black hole sources, where both black holes produced a jet at some point, or spin flips after a black hole merger (Merritt & Ekers 2002). A recent study of X-shaped sources has found that four per cent of all radio sources need to re-orient black hole spin during the radio source lifetime (Saripalli & Roberts 2018).

Observations of the host galaxies support this picture. Radio-loud and thus jet-producing supermassive black holes are frequently found in interacting galaxies (Shabala et al. 2012; Ramos Almeida et al. 2013; Sabater, Best & Argudo-Fernández 2013). When two black holes approach each other, they expel stars, thus imprinting a core profile on the stellar density structure. Galaxies with core profiles show enhanced radio loudness (Richings, Uttley & Körding 2011). Near infrared observations with the upcoming *James Webb Space Telescope* might be able to address this connection for part of our sample of powerful radio galaxies.

X-ray cavities around radio sources in general are distributed almost isotropically which is consistent with the idea that binary supermassive black holes play an important role with precession and black hole mergers re-orienting spins frequently (Babul, Sharma & Reynolds 2013; Cielo et al. 2018).

One might expect kinematic signatures of supermassive black hole binaries to appear in their broad emission lines. We searched the literature for complementary data for the radio sources discussed here. The only sources with double-peaked broad emission lines are 3C 382 and 3C 390.3 (classified above as precessing, Eracleous & Halpern 2003; Liu, Eracleous & Halpern 2016). 3C 47, 3C 234, 3C 249.1, and 3C 334, two of which are classified as non-precessing above, are single-peaked emitters (Eracleous & Halpern 2003). However, based on multi-epoch spectroscopy, Liu et al. (2016) and Eracleous & Halpern (2003) reject the binary black hole hypothesis as the explanation for their double-peaked objects. Liu et al. (2016) extend this conclusion to double-peaked broad-line emitters in general, which is confirmed by other studies (e.g. Wang et al. 2017). 3C 390.3 has, however, been found to have a

Table 3. Gravitational wave emission from nearby binary black hole candidates. d_L: luminosity distance. M_9: total black hole mass in units of $10^9 \, M_\odot$. P_{gp}: estimated geodetic precession period. h_0: prediction for the gravitational wave strain amplitude. For Cygnus A, we adopt a reference separation of 0.3 ± 0.25 pc. Details for the individual sources are discussed in Appendix C.

Source	d_L/Mpc	M_9	P_{gp}/Myr	$h_0/10^{-17}$
Centaurus A	11	0.055 ± 0.01	1 ± 0.5	0.6 ± 0.5
Cygnus A	237	2.5 ± 0.3	1.75 ± 1.25	4.1 ± 4.7
Hydra A	240	0.5 ± 0.4	1 ± 0.5	0.5 ± 0.5
Virgo A / M87	22.2	6.6 ± 0.4	6 ± 2	113 ± 113

periodicity in its optical light curve of about 10 yr (Kovačević et al. 2018), which could be related to the orbital period of a supermassive binary (Charisi et al. 2016). Precession studies are sensitive to supermassive binaries with very unequal masses, so that the secondary might frequently be too faint to appear spectroscopically. Also, subparsec separations as suggested here are comparable to the size of the broad-line region (Kaspi et al. 2000). The kinematics of broad-line regions in general is not fully understood with radiation pressure and other factors likely playing a role (Eracleous & Halpern 2003; Marconi et al. 2008; Netzer & Marziani 2010; Krause, Burkert & Schartmann 2011; Krause, Schartmann & Burkert 2012a; Liu et al. 2016). We would therefore not expect that two distinct broad-line regions would be identifiable for our objects.

4.5 Possible gravitational wave detections for nearby extragalactic radio sources

Final confirmation of our proposed binary supermassive black hole candidates would require a gravitational wave detection. Unfortunately, the signal will likely be too weak to expect detections in the near future. We exemplify this with the closest sources for which jet precession could be argued for from their radio images.

The characteristic strain amplitude for a source at a distance of $d_{L, Gpc} 10^9$ pc precessing with a period $P_{gp, Myr} 10^6$ yr is given by (Zhu et al. 2015)

$$h_0 = 1.12 \times 10^{-18} \, (f_r/0.0357) \, d_{L,Gpc}^{-1} \, M_9^{7/5} \, P_{gp,Myr}^{-2/5} , \qquad (5)$$

where $f_r^5 = r^3 (1 + r)^{-6} (3r + 4)^{-2}$. The closest jet sources display ample signs of binary black holes, e.g. precession in Hydra A where a simulation study has constrained the period to 1 Myr (Nawaz et al. 2016). We give details of the best candidates for gravitational wave detections in Appendix C and summarize best estimates for h_0 in Table 3. They are generally of the order of 10^{-17} except for M87 (a core elliptical Côté et al. 2006), where h_0 could be as high as 10^{-15}. Pulsar timing with the Square Kilometre Array radio telescope is expected to detect gravitational waves at relevant frequencies down to $h_0 = 6 \times 10^{-16}$ (Lazio 2013). The SKA pulsar timing array is currently the best observatory on the horizon for such observations. Unfortunately, this means that we can hardly expect an independent confirmation of our binary supermassive black hole candidates by individual gravitational wave detections. This is in contrast to more optimistic predictions based on the ILLUSTRIS cosmological simulation (Kelley et al. 2018). A detection for M87 appears possible, but we caution that this is perhaps the least secure of the binary black hole candidates we discuss in Appendix C. We also note that the black-hole mass of M87 may be lower than our presently adopted value based on stellar-dynamical models. Indeed the recent finding of a substantial increase in the stellar mass-to-light ratio towards the centre of M87 (relating to variations in the stellar initial mass function; Sarzi et al. 2018) may eventually lead to a downward revision of the black hole mass in this galaxy, which

would also better agree with the gas-dynamical measurements (e.g. Walsh et al. 2013). Because the gravitational wave strain depends superlinearly on the total mass of a binary (compare equation 5), this would make the detection of a gravitational wave signal even less likely.

5 CONCLUSIONS

Supermassive black hole binaries are predicted in hierarchical cosmological evolution. Sophisticated galaxy merger simulations that treat the relativistic physics of the supermassive black holes predict subparsec separations for time-scales comparable to radio source lifetimes or longer (Khan et al. 2016; Mayer 2017). If such a source had a radio jet, two effects would be predicted (compare Section 1, Begelman et al. 1980): (1) a comparatively short-term precession likely observable with VLBI multi-epoch imaging, and (2) a long-term precession, which can potentially be observed as morphological features on VLA radio maps.

For one of the best-studied extragalactic radio sources, Cygnus A, we find evidence for precession in the VLA radio map with a period of about 0.5–3 Myr. A helical structure exists on the parsec scale that could be produced by a supermassive black hole binary with an orbital time-scale of 18 yr. Both observations are consistent with a subparsec supermassive binary. The observations are, however, inconclusive regarding the mass ratio of the binary.

We have shown that morphological features in kiloparsec-scale, VLA radio maps of 3CRR radio sources are very frequently (73 per cent) consistent with jet precession with a time-scale of the order of 10^6–10^7 yr. We argue that the likely cause for the jet precession in these radio sources is geodetic precession in a close binary black hole system. Precession of the black hole spins due to interaction with a massive accretion disc would predict a single precession cycle. Radio morphologies suggest, however, multiple cycles. The single precession cycle would likely occur at the beginning of an active phase, but we find precession frequently also for sources older than 100 Myr. With reasonable assumptions about the black hole masses, the geodetic precession interpretation requires supermassive black hole binaries with separations $\lesssim 1$ pc in these powerful extragalactic jet sources. We support the precession interpretation with additional pieces of circumstantial evidence.

While the parsec-scale structure has not been systematically studied for our sample of 100 kpc scale radio sources, analogous samples of powerful parsec-scale jet sources exist, for example the MOJAVE samples (Lister et al. 2013). Essentially all of these sources show evidence of significant variation of the innermost jet direction over the time-scale covered by current multi-epoch observations over 12–16 yr, as shown by Lister et al. (2013). Jet angle variations have been linked to orbital motion of binary black holes by Lobanov & Roland (2005).

There is therefore evidence for both effects expected if the jets are produced in close binary black holes, namely orbital and geodetic

precession. Our results for the 100-kpc scale radio sources showed that at least 73 per cent of these sources show evidence for precessing jets. The MOJAVE results may hint at an even higher fraction. Indeed, since we conservatively required two precession features for a firm assignment of precession, there could be more precessing sources which are not picked up by our analysis.

The high fraction of close binary black holes in powerful jet sources might suggest that supermassive black holes in general are very likely to occur as a binary system. As the merger time-scale due to gravitational wave emission and interaction with stars is expected to be significantly shorter than the Hubble time (Begelman et al. 1980; Khan et al. 2016; Mayer 2017), this may imply a steady influx of black holes probably from minor galaxy mergers. Recent cosmological simulations predict that a significant number of supermassive black holes will be present in a given galaxy at any one time (Tremmel et al. 2018b). How fast they approach each other depends on the spatial distribution of stars within the galaxy (Tremmel et al. 2018a).

The alternative interpretation would be that binary black hole formation and jet formation are somehow linked. One possibility could be that galaxy mergers would cause both, the close approach of the supermassive black holes and the accretion of gas into the centre of the merged galaxy with subsequent jet formation.

Independent confirmation of our subparsec binary supermassive black hole candidates, and in fact any extragalactic jet source with some evidence for geodetic precession, via individual gravitational wave detections will be difficult. We estimate the gravitational wave strain for the closest jet sources with some evidence for binary black holes from precession. The only source where the SKA pulsar timing array could have some hope for detection is M87. Thus, improved modelling of the jet–environment interaction for precessing jet sources is probably the best way to better constrain powerful objects in the coming years.

ACKNOWLEDGEMENTS

REFERENCES

Abbott B. P. et al., 2016, Phys. Rev. Lett., 116, 061102
Abraham Z., Carrara E. A., 1998, ApJ, 496, 172
Alexander P., 1985, MNRAS, 213, 743
Alexander P., Pooley G. G., 1996, in Carilli C. L., Harris D. E., eds, Cygnus A – Study of a Radio Galaxy. Cambridge Univ. Press, Cambridge
Aloy M. A., Ibáñez J. M., Martí J. M., Gómez J.-L., Müller E., 1999, ApJ, 523, L125
Amaro-Seoane P. et al., 2012, Class. Quantum Gravity, 29, 124016
Appl S., 1996, A&A, 314, 995
Appl S., Sol H., Vicente L., 1996a, in Hardee P. E., Bridle A. H., Zensus J. A., eds, ASP Conf. Ser. Vol. 100, Energy Transport in Radio Galaxies and Quasars. Astron. Soc. Pac., San Francisco, p. 181
Appl S., Sol H., Vicente L., 1996b, A&A, 310, 419
Babul A., Sharma P., Reynolds C. S., 2013, ApJ, 768, 11
Balsara D. S., Norman M. L., 1992, ApJ, 393, 631
Bansal K., Taylor G. B., Peck A. B., Zavala R. T., Romani R. W., 2017, ApJ, 843, 14
Bardeen J. M., Petterson J. A., 1975, ApJ, 195, L65
Barker B. M., O'Connell R. F., 1975, ApJ, 199, L25
Baryshev Y. V., 1983, Sov. Astron. Lett., 9, 307
Beckwith K., Hawley J. F., Krolik J. H., 2008, ApJ, 678, 1180
Begelman M. C., Blandford R. D., Rees M. J., 1980, Nature, 287, 307
Begelman M. C., Blandford R. D., Rees M. J., 1984, Rev. Mod. Phys., 56, 255
Black A. R. S., Baum S. A., Leahy J. P., Perley R. A., Riley J. M., Scheuer P. A. G., 1992, MNRAS, 256, 186
Boccardi B., Krichbaum T. P., Bach U., Ros E., Zensus A. J., 2014, in Proc. Sci., 12th European VLBI Network Symposium and Users Meeting (EVN 2014)016
Boccardi B., Krichbaum T. P., Bach U., Mertens F., Ros E., Alef W., Zensus J. A., 2016a, A&A, 585, A33
Boccardi B., Krichbaum T. P., Bach U., Bremer M., Zensus J. A., 2016b, A&A, 588, L9
Bogdán Á., Lovisari L., Volonteri M., Dubois Y., 2018, ApJ, 852, 131
Britzen S. et al., 2017, A&A, 602, A29
Cappellari M., Neumayer N., Reunanen J., van der Werf P. P., de Zeeuw P. T., Rix H.-W., 2009, MNRAS, 394, 660
Capuzzo-Dolcetta R., Tosta e Melo I., 2017, MNRAS, 472, 4013
Carilli C. L., Barthel P. D., 1996, A&AR, 7, 1
Carilli C. L., Kurk J. D., van der Werf P. P., Perley R. A., Miley G. K., 1999, AJ, 118, 2581
Charisi M., Bartos I., Haiman Z., Price-Whelan A. M., Graham M. J., Bellm E. C., Laher R. R., Márka S., 2016, MNRAS, 463, 2145
Chiaberge M. et al., 2017, A&A, 600, A57
Choi E., Wiita P. J., Ryu D., 2007, ApJ, 655, 769
Chon G., Böhringer H., 2017, A&A, 606, L4
Chon G., Böhringer H., Krause M., Trümper J., 2012, A&A, 545, L3
Cielo S., Babul A., Antonuccio-Delogu V., Silk J., Volonteri M., 2018, A&A, 617, A58
Côté P. et al., 2006, ApJS, 165, 57
Cox C. I., Gull S. F., Scheuer P. A. G., 1991, MNRAS, 252, 558
Croston J. H. et al., 2009, MNRAS, 395, 1999
Dabbech A., Onose A., Abdulaziz A., Perley R. A., Smirnov O. M., Wiaux Y., 2018, MNRAS, 476, 2853
De Villiers J., Hawley J. F., Krolik J. H., 2003, ApJ, 599, 1238
Donohoe J., Smith M. D., 2016, MNRAS, 458, 558
Ekers R. D., 2014, in Meiron Y., Li S., Liu F.-K., Spurzem R., eds, Proc. IAU Symp. S312, Vol. 10, Star Clusters and Black Holes in Galaxies across Cosmic Time. Cambridge Univ. Press, Cambridge, UK, p. 26
Ekers R. D., Fanti R., Lari C., Parma P., 1978, Nature, 276, 588
English W., Hardcastle M. J., Krause M. G. H., 2016, MNRAS, 461, 2025
Eracleous M., Halpern J. P., 2003, ApJ, 599, 886
Fanaroff B. L., Riley J. M., 1974, MNRAS, 167, 31P
Fender R. P., Gallo E., Russell D., 2010, MNRAS, 406, 1425
Gaibler V., Khochfar S., Krause M., 2011, MNRAS, 411, 155
Gaibler V., Khochfar S., Krause M., Silk J., 2012, MNRAS, 425, 438

Gardner E., Done C., 2018, MNRAS, 473, 2639

Gebhardt K., Adams J., Richstone D., Lauer T. R., Faber S. M., Gültekin K., Murphy J., Tremaine S., 2011, ApJ, 729, 119

Ghisellini G., Tavecchio F., Maraschi L., Celotti A., Sbarrato T., 2014, Nature, 515, 376

Gilbert G. M., Riley J. M., Hardcastle M. J., Croston J. H., Pooley G. G., Alexander P., 2004, MNRAS, 351, 845

Gower A. C., Hutchings J. B., 1982, ApJ, 258, L63

Gower A. C., Gregory P. C., Unruh W. G., Hutchings J. B., 1982, ApJ, 262, 478

Graham M. J. et al., 2015, MNRAS, 453, 1562

Hardcastle M. J., Alexander P., Pooley G. G., Riley J. M., 1997, MNRAS, 288, 859

Hardcastle M. J., Alexander P., Pooley G. G., Riley J. M., 1998, MNRAS, 296, 445

Hardcastle M. J. et al., 2007, ApJ, 670, L81

Hardee P. E., Norman M. L., 1990, ApJ, 365, 134

Häring N., Rix H.-W., 2004, ApJ, 604, L89

Harwood J. J. et al., 2017, MNRAS, 469, 639

Hines D. C., Owen F. N., Eilek J. A., 1989, ApJ, 347, 713

Hutchings J. B., Price R., Gower A. C., 1988, ApJ, 329, 122

Jorstad S. G., Marscher A. P., Lister M. L., Stirling A. M., Cawthorne T. V., Gómez J.-L., Gear W. K., 2004, AJ, 127, 3115

Kaiser C. R., Alexander P., 1999, MNRAS, 305, 707

Kaspi S., Smith P. S., Netzer H., Maoz D., Jannuzi B. T., Giveon U., 2000, ApJ, 533, 631

Kelley L. Z., Blecha L., Hernquist L., Sesana A., Taylor S. R., 2018, MNRAS, 477, 964

Khan F. M., Fiacconi D., Mayer L., Berczik P., Just A., 2016, ApJ, 828, 73

Kharb P., Lister M. L., Cooper N. J., 2010, ApJ, 710, 764

Kharb P., O'Dea C. P., Baum S. A., Hardcastle M. J., Croston J. H., Mingo B., Noel-Storr J., 2014, MNRAS, 440, 2976

Kharb P., Lal D. V., Merritt D., 2017, Nat. Astron., 1, 727

Koide S., Meier D. L., Shibata K., Kudoh T., 2000, ApJ, 536, 668

Komissarov S. S., McKinney J. C., 2007, MNRAS, 377, L49

Komissarov S. S., Barkov M. V., Vlahakis N., Königl A., 2007, MNRAS, 380, 51

Komossa S., Burwitz V., Hasinger G., Predehl P., Kaastra J. S., Ikebe Y., 2003, ApJ, 582, L15

Kovačević A. B., Pérez-Hernández E., Popović L. Č., Shapovalova A. I., Kollatschny W., Ilić D., 2018, MNRAS, 475, 2051

Kraft R. P., Hardcastle M. J., Worrall D. M., Murray S. S., 2005, ApJ, 622, 149

Krause M., 2003, A&A, 398, 113

Krause M., 2005, A&A, 431, 45

Krause M., Camenzind M., 2001, A&A, 380, 789

Krause M., Burkert A., Schartmann M., 2011, MNRAS, 411, 550

Krause M., Schartmann M., Burkert A., 2012a, MNRAS, 425, 3172

Krause M., Alexander P., Riley J., Hopton D., 2012b, MNRAS, 427, 3196

Kun E., Gabányi K. É., Karouzos M., Britzen S., Gergely L. Á., 2014, MNRAS, 445, 1370

Kun E., Frey S., Gabányi K. É., Britzen S., Cseh D., Gergely L. Á., 2015, MNRAS, 454, 1290

Laing R. A., Riley J. M., Longair M. S., 1983, MNRAS, 204, 151

Lazio T. J. W., 2013, Class. Quantum Gravity, 30, 224011

Lazio T. J. W., Cohen A. S., Kassim N. E., Perley R. A., Erickson W. C., Carilli C. L., Crane P. C., 2006, ApJ, 642, L33

Leahy J. P., Black A. R. S., Dennett-Thorpe J., Hardcastle M. J., Komissarov S., Perley R. A., Riley J. M., Scheuer P. A. G., 1997, MNRAS, 291, 20

Li Y.-R. et al., 2016, ApJ, 822, 4

Lister M., 2016, Galaxies, 4, 29

Lister M. L. et al., 2013, AJ, 146, 120

Liu J., Eracleous M., Halpern J. P., 2016, ApJ, 817, 42

Lobanov A. P., Roland J., 2005, A&A, 431, 831

Lodato G., Pringle J. E., 2006, MNRAS, 368, 1196

Lu R.-S. et al., 2013, ApJ, 772, 13

McKean J. P. et al., 2016, MNRAS, 463, 3143

Magorrian J. et al., 1998, AJ, 115, 2285

Marconi A., Schreier E. J., Koekemoer A., Capetti A., Axon D., Macchetto D., Caon N., 2000, ApJ, 528, 276

Marconi A., Axon D. J., Maiolino R., Nagao T., Pastorini G., Pietrini P., Robinson A., Torricelli G., 2008, ApJ, 678, 693

Mayer L., 2017, J. Phys. Conf. Ser., 840, 012025

Merritt D., Ekers R. D., 2002, Science, 297, 1310

Moderski R., Sikora M., Lasota J., 1998, MNRAS, 301, 142

Monceau-Baroux R., Porth O., Meliani Z., Keppens R., 2014, A&A, 561, A30

Morganti R., Oosterloo T., Tadhunter C. N., Aiudi R., Jones P., Villar-Martin M., 1999a, A&AS, 140, 355

Morganti R., Killeen N. E. B., Ekers R. D., Oosterloo T. A., 1999b, MNRAS, 307, 750

Mukherjee D., Bicknell G. V., Sutherland R., Wagner A., 2016, MNRAS, 461, 967

Müller C. et al., 2014, A&A, 569, A115

Mullin L. M., Hardcastle M. J., Riley J. M., 2006, MNRAS, 372, 113

Mullin L. M., Riley J. M., Hardcastle M. J., 2008, MNRAS, 390, 595

Nawaz M. A., Bicknell G. V., Wagner A. Y., Sutherland R. S., McNamara B. R., 2016, MNRAS, 458, 802

Netzer H., Marziani P., 2010, ApJ, 724, 318

O'Neill S. M., Beckwith K., Begelman M. C., 2012, MNRAS, 422, 1436

Owen F. N., Eilek J. A., Kassim N. E., 2000, ApJ, 543, 611

Perley D. A., Perley R. A., Dhawan V., Carilli C. L., 2017, ApJ, 841, 117

Perucho M., Martí J. M., Hanasz M., 2004, A&A, 427, 431

Perucho M., Martí J. M., Cela J. M., Hanasz M., de La Cruz R., Rubio F., 2010, A&A, 519, A41

Peterson B. M. et al., 2004, ApJ, 613, 682

Porth O., Fendt C., 2010, ApJ, 709, 1100

Rafferty D. A., McNamara B. R., Nulsen P. E. J., Wise M. W., 2006, ApJ, 652, 216

Ramos Almeida C., Bessiere P. S., Tadhunter C. N., Inskip K. J., Morganti R., Dicken D., González-Serrano J. I., Holt J., 2013, MNRAS, 436, 997

Richings A. J., Uttley P., Körding E., 2011, MNRAS, 415, 2158

Rieger F. M., 2007, Ap&SS, 309, 271

Rodriguez-Gomez V. et al., 2015, MNRAS, 449, 49

Rodríguez-Martínez M., Velázquez P. F., Binette L., Raga A. C., 2006, A&A, 448, 15

Rosen A., Hardee P. E., Clarke D. A., Johnson A., 1999a, ApJ, 510, 136

Rosen A., Hughes P. A., Duncan G. C., Hardee P. E., 1999b, ApJ, 516, 729

Rossi P., Bodo G., Capetti A., Massaglia S., 2017, A&A, 606, A57

Sabater J., Best P. N., Argudo-Fernández M., 2013, MNRAS, 430, 638

Saripalli L., Roberts D. H., 2018, ApJ, 852, 48

Sarzi M., Spiniello C., La Barbera F., Krajnović D., van den Bosch R., 2018, MNRAS, 478, 4084

Savolainen T., Wiik K., Valtaoja E., Tornikoski M., 2006, A&A, 446, 71

Scheuer P. A. G., 1982, in Heeschen D. S., Wade C. M., eds, Proc. IAU Symp. 97, Extragalactic Radio Sources. D. Reidel Publishing Co., Dordrecht, p. 163

Scheuer P. A. G., Feiler R., 1996, MNRAS, 282, 291

Shabala S. S. et al., 2012, MNRAS, 423, 59

Smith D. A., Wilson A. S., Arnaud K. A., Terashima Y., Young A. J., 2002, ApJ, 565, 195

Stairs I. H., 2003, Living Rev. Relat., 6, 5

Steenbrugge K. C., Blundell K. M., 2008, MNRAS, 388, 1457

Tadhunter C., Marconi A., Axon D., Wills K., Robinson T. G., Jackson N., 2003, MNRAS, 342, 861

Taylor G. B., 1996, ApJ, 470, 394

Taylor G. B., Perley R. A., Inoue M., Kato T., Tabara H., Aizu K., 1990, ApJ, 360, 41

Thorne K. S., Blandford R. D., 2017, Modern Classical Physics: Optics, Fluids, Plasmas, Elasticity, Relativity, and Statistical Physics. Princeton Univ. Press, Princeton, NJ

Tremmel M., Governato F., Volonteri M., Quinn T. R., Pontzen A., 2018a, MNRAS, 475, 4967

Tremmel M., Governato F., Volonteri M., Pontzen A., Quinn T. R., 2018b, ApJ, 857, L22

Turner R. J., Shabala S. S., Krause M. G. H., 2018, MNRAS, 474, 3361

Wagner A. Y., Bicknell G. V., 2011, ApJ, 728, 29
Wagner A. Y., Bicknell G. V., Umemura M., 2012, ApJ, 757, 136
Wall J. V., Peacock J. A., 1985, MNRAS, 216, 173
Walsh J. L., Barth A. J., Ho L. C., Sarzi M., 2013, ApJ, 770, 86
Wang L., Greene J. E., Ju W., Rafikov R. R., Ruan J. J., Schneider D. P., 2017, ApJ, 834, 129
Weijmans A.-M. et al., 2014, MNRAS, 444, 3340
Williams A. G., Gull S. F., 1985, Nature, 313, 34
Wilson A. S., Young A. J., Shopbell P. L., 2000, ApJ, 544, L27
Zhu X.-J. et al., 2015, MNRAS, 449, 1650

APPENDIX A: COMPARISON BETWEEN BALLISTIC JET MODELS AND HYDRODYNAMIC SIMULATIONS

Hydrodynamic effects in radio lobes have been shown to be able to bend also non-precessing jets (Hardee & Norman 1990). This is especially important close to the terminal hotspots, where lobe pressures are high. To investigate the role of the hydrodynamic

Table A1. Parameters for the jet models compared in Fig. A1.

Parameter	Simulation	Ballistic model
Jet velocity	$0.8c$	$0.1c$
Precession period	1 Myr	0.85 Myr
Inclination from line of sight	$42°$	$42°$
Starting angle of precession[a]	$-45°$	$-45°$
Prec. cone half opening angle	$20°$	$10°$

[a] Ωt_{ref} in Gower et al. (1982).

effects, we compare a 3D hydrodynamic simulation, published in Nawaz et al. (2016), to a ballistic jet model (Gower et al. 1982) for the precessing jet source Hydra A in Fig. A1. Model parameters are given in Table A1. It is clear that even for this comparatively low-power jet, the curvature induced by precession dominates the observational appearance for most of the region where the jet is observed. It is therefore reasonable to take curvature as signature for precessing jets.
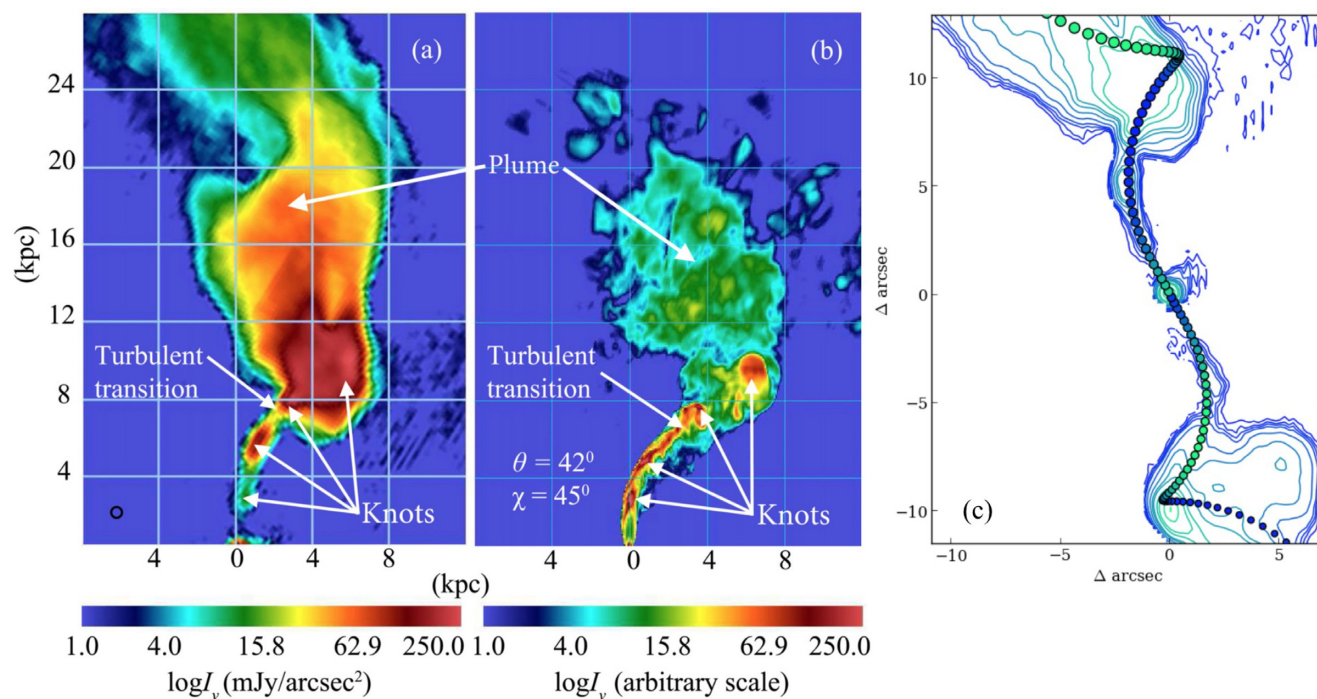
Figure A1. Different methods of modelling the precessing jet in Hydra A. (a) VLA image of Hydra A. (b) Hydrodynamic simulation of a jet with parameters empirically matched to Hydra A. (c) Ballistic jet model (Gower et al. 1982) for Hydra A. Even though Hydra A has a weaker jet than the powerful jet sources discussed elsewhere in this article, the jet path is over most of its length well modelled by the hydrodynamic simulation as well as the ballistic model. This suggests that precession effects are indeed observable in real radio sources. Panels (a) and (b) were adopted from Nawaz et al. (2016).

APPENDIX B: RADIO MAPS FOR THE COMPLETE SAMPLE

We provide here all the radio maps of our complete sample. Shown is Stokes I in Jy beam^{-1}. The mapping of the flux levels onto the colour map is non-linear and has been adjusted carefully for each map to ensure lobe and jet structures are well visible. Equatorial coordinates are given on the maps. Observing frequency, resolution, redshift, and precession indicators are given in the individual figure captions. The features of precessing jets are indicated on each map if applicable.
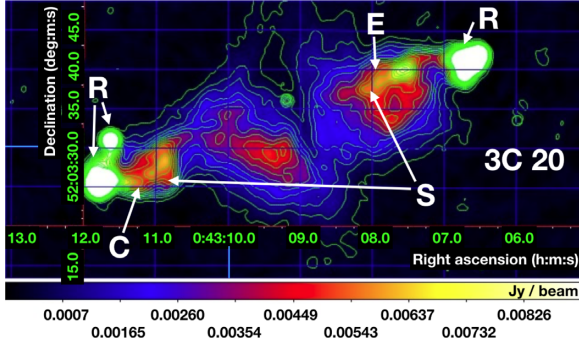
Figure B1. 3C 20, 8.41 GHz, resolution: 1″.1, redshift: 0.174. C: Curved jet structure on the eastern side. E: Lobe brightness asymmetry/jet at edge of lobe on the western side. R: Multiple terminal hotspots on the eastern side; wide terminal hotspot on the western side. S: S-symmetry. Additionally, interaction with ambient medium.
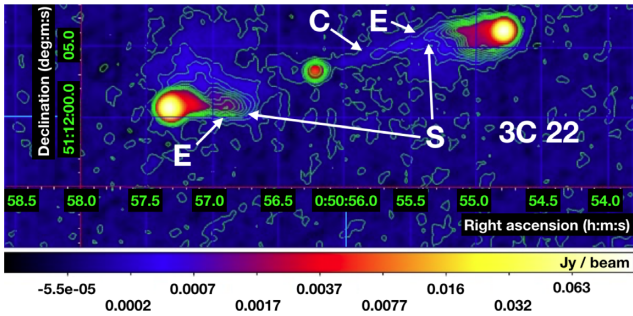
Figure B2. 3C 22, 8.56 GHz, resolution: 0″.75, redshift: 0.938. C: Curved jet. E: Misaligned lobe axis on the eastern side. Lobe brightness asymmetry on the western side. S: S symmetric jets.
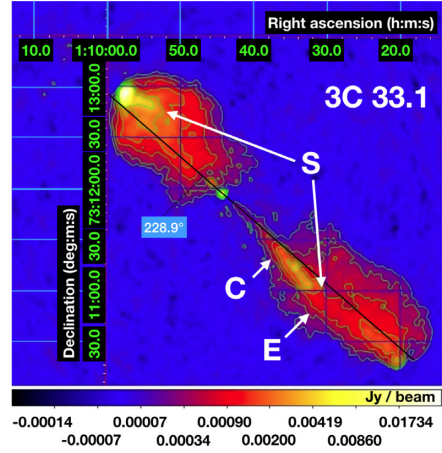
Figure B3. 3C 33.1, 4.85 GHz, resolution: 2″.948 × 2″.472, redshift: 0.18. C: Curved eastern jet. E: Misaligned lobe axis on the eastern side. S: S-symmetric jets. Jet enters lobe on southern side. Jet bends with brightening, possibly related to jet–cloud interaction. Southern tip-of-lobe hotspot lies along the continuation of inner southern jet. The innermost part of the jets is aligned with the lobe axis [solid black line, position angle (jet side) indicated].
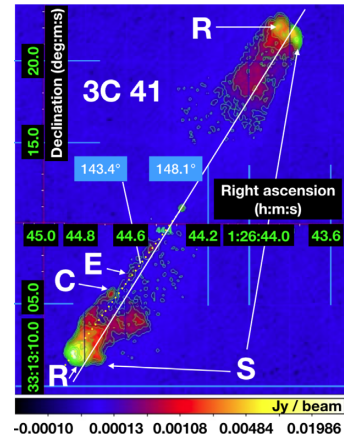
Figure B4. 3C 41, 8.46 GHz, resolution: 0″.2, redshift: 0.795. C: Curved southern jet. E: Misaligned lobe. R: Wide terminal hotspots on both sides. S: S-symmetric jet–hotspots. Southern jet (yellow dotted line) misaligned with lobe axis (solid white line) by 5°.
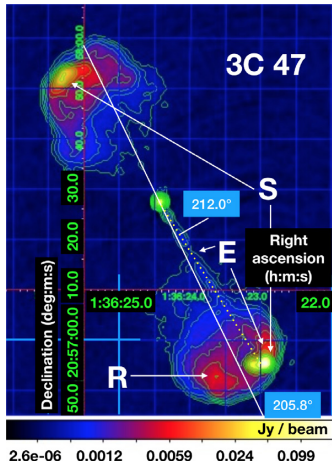
Figure B5. 3C 47, 4.89 GHz, resolution: 1″3, redshift: 0.43. E: Jet and hotspots at edge of lobe. R: Ring structure near hotspot. S: S-symmetry. Jet (yellow dotted line) misaligned with lobe axis by 6°.
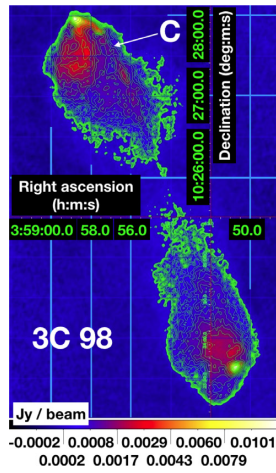
Figure B6. 3C 98, 8.35 GHz, resolution: 2″, redshift: 0.03. C: The outer part of the northern jet is curved, possibly related to precession. Jet and hotspot at one side of lobe, but possibly due to interaction with ambient medium.
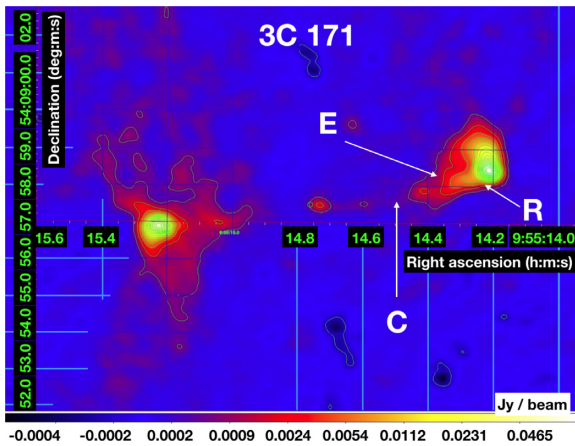
Figure B7. 3C 171, 8.06 GHz, resolution: 0″35 × 0″25, redshift: 0.24. C: Curved eastern jet. E: Misaligned lobe axis on the eastern side. R: Wide terminal hotspot on the eastern side. Image quality is not very good and the source has complex structure.
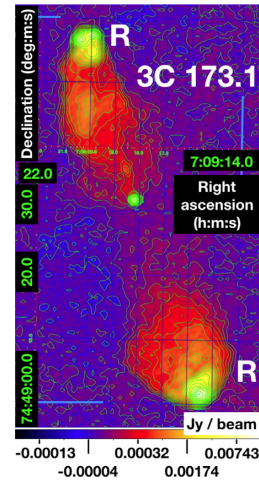
Figure B8. 3C 173.1, 8.44 GHz, resolution: 0″75, redshift: 0.292. R: Double hotspot in the north, extended hotspot in the south. Moderate bend in northern lobe structure. Otherwise the source appears simple and symmetric.
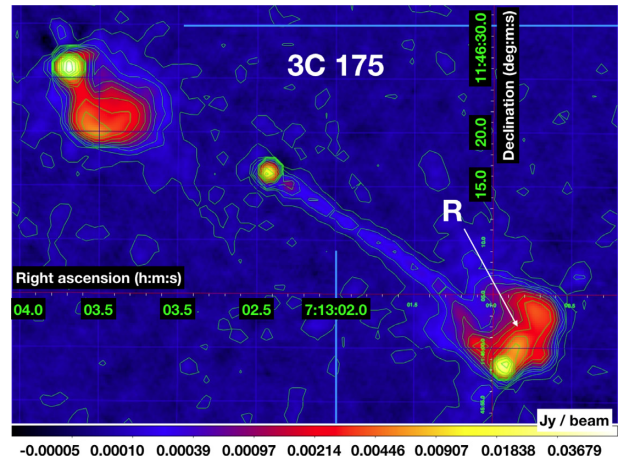
Figure B9. 3C 175, 8.45 GHz, resolution: 1″0, redshift: 0.768. R: Some evidence of ring structure, clearer in southern hotspot. Jet mainly in the middle of the lobe, bends south towards hotspot at edge of lobe. Since the bend is at the tip of the lobe, this could be due to hydrodynamic effects.
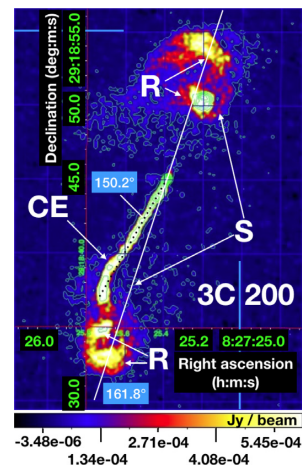
Figure B10. 3C 200, 8.46 GHz, resolution: 0″25, redshift: 0.46. CE: Curved jet at the edge of southern lobe. R: Ring-like structure for both hotspots. S: Clear S-symmetry. Jet misaligned with lobe axis by 12°.
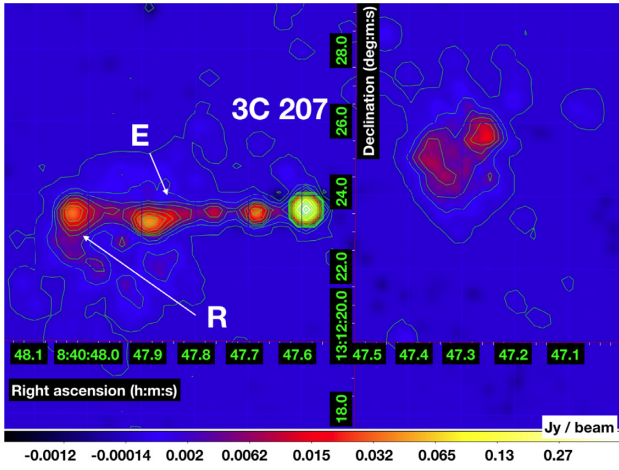
Figure B11. 3C 207, 4.86 GHz, resolution: 0.''35, redshift: 0.90. E: Jet/lobe misalignment on eastern side. R: Wide hotspot on eastern side. Faint lobe.
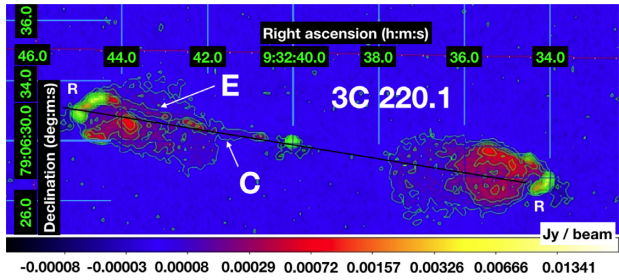
Figure B12. 3C 220.1, 8.44 GHz, resolution: 0.''25, redshift: 0.61. C: Curvature of jet on the western side, E: Jets at edge of lobes, R: Wide terminal hotspots on both sides; ring-like feature at eastern hotspot.
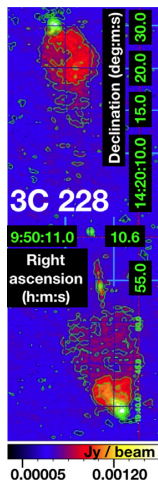
Figure B13. 3C 228, 8.47 GHz, resolution: 0.''225, redshift: 0.55. Hotspots, jet, and core perfectly aligned.
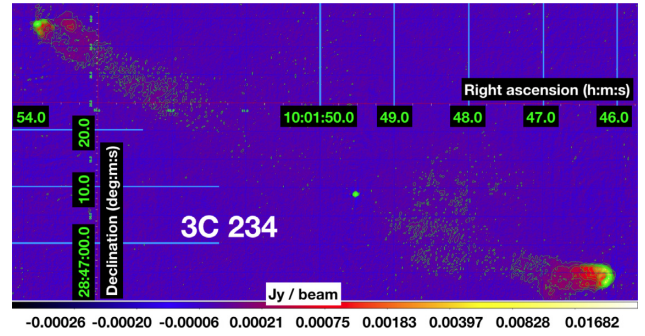
Figure B14. 3C 234, 8.44 GHz, resolution: 0.''3, redshift: 0.18. Wide central, low surface brightness, structure could indicate interaction with dense host ISM. Deviation in lobe direction could point to interaction with neighbouring galaxy. Complex structure, no evidence for precession.
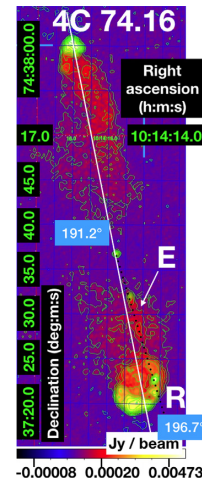
Figure B15. 4C 74.16, 8.47 GHz, resolution: 0.''3, redshift: 0.81. E: Jet runs into lobe along its edge, R: Partial ring structure in the southern lobe, Wiggles in the northern lobes which is not part of our classification scheme. The angle between jet (black dotted line) and lobe axis (white solid line) is 6°.
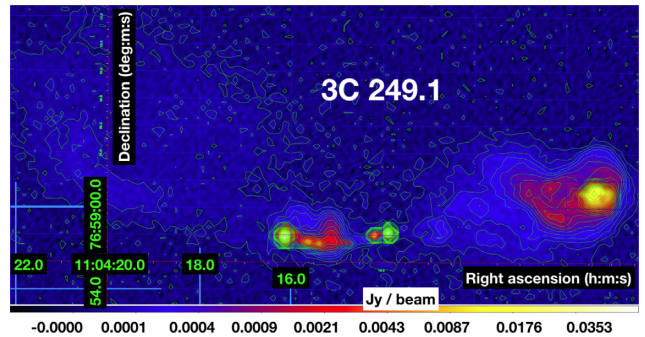
Figure B16. 3C 249.1, 4.89 GHz, resolution: 0.''35, redshift: 0.31. Complex structure. Bent at a bright spot, pointing to persistent jet–cloud (jet–galaxy) interaction. Crosswind from south. The source structure is too complex for firm diagnosis of precession signatures.
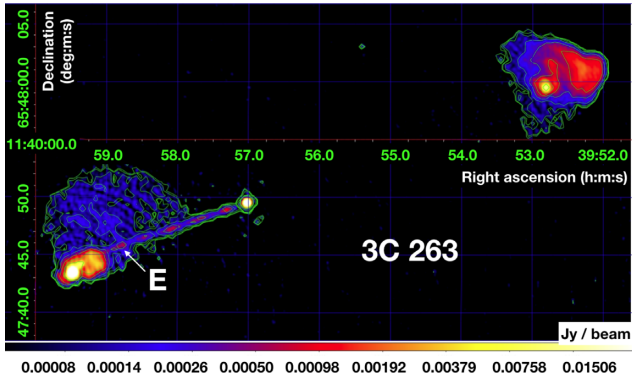
Figure B17. 3C 263, 4.86 GHz, resolution: 0″.35, redshift: 0.65. E: Misaligned lobe axis on the eastern side.
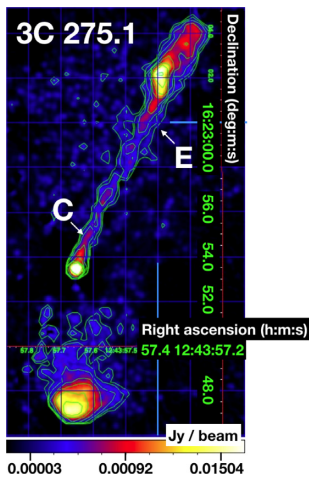
Figure B18. 3C 275.1, 8.46 GHz, resolution: 0″.225, redshift: 0.42. C: Jet is curved, E: Jet is not symmetric with respect to lobe axis (either northern or southern jet as implied by the southern hotspot position). Northern lobe almost lost in noise. We can therefore not assign a misalignment angle with confidence.
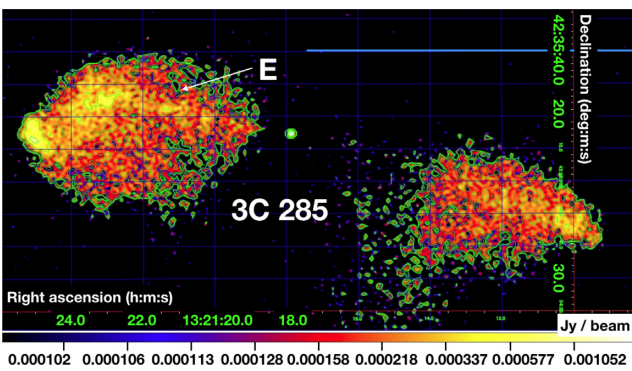
Figure B19. 3C 285, 4.87 GHz, resolution: 1″, redshift: 0.079. E: Jet at edge of lobes. Indication for motion through ICM roughly perpendicular to jet axis. Northern jet axis differs from southern jet axis. Possible interaction near tip of north lobe.
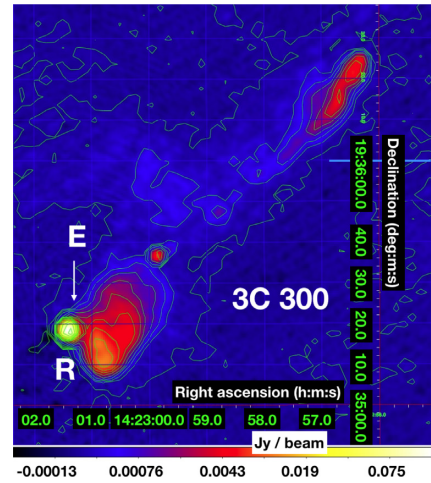
Figure B20. 3C 300, 8.06 GHz, resolution: 2″.1, redshift: 0.27. E: Hotspot/lobe misalignment southern lobe. R: Wide/multiple southern hotspot.
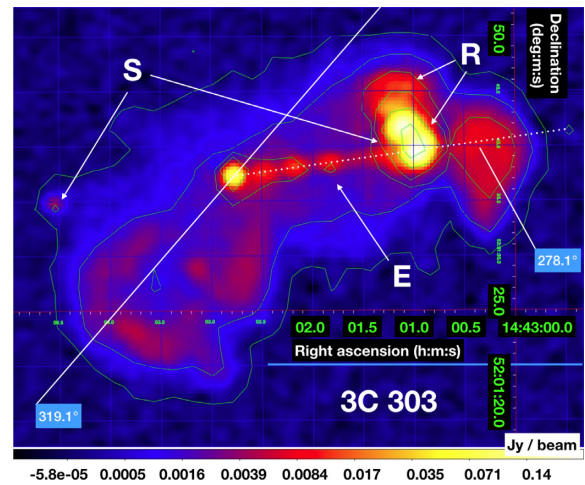
Figure B21. 3C 3C 303, 1.45 GHz, resolution: 1″.2, redshift: 0.141. E: Misaligned lobe axis on the western side. R: Multiple terminal hotspots on the western side. S: S-symmetric hotspots.
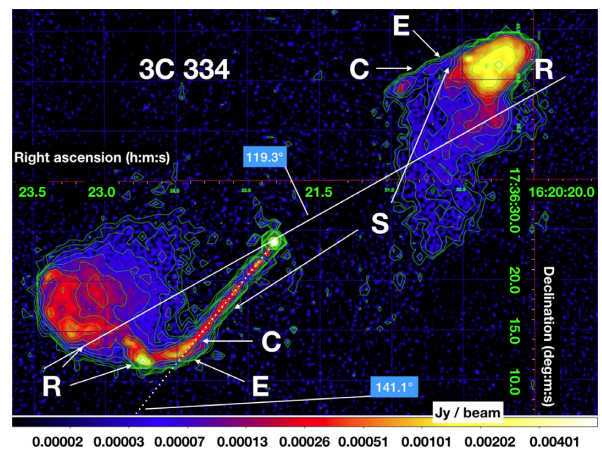
Figure B22. 3C 334, 4.89 GHz, resolution: 0″.35, redshift: 0.555. C: Curved jets. E: Misaligned lobe axis on both sides. R: Wide terminal hotspots on western side; ring-shaped feature at hotspot on eastern side. S: S-symmetric jet–lobe structure.
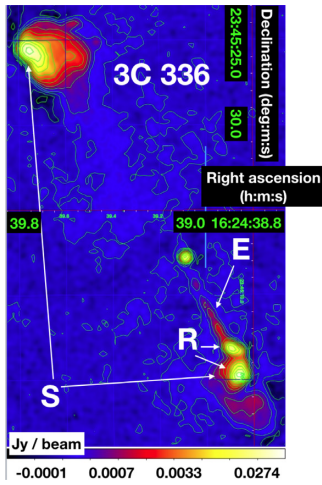
Figure B23. 3C 336, 4.86 GHz, resolution: 0.″35, redshift: 0.93. E: Misaligned lobe axis on both sides, R: Multiple terminal hotspots on the southern side, S: S-symmetric jet–hotspots.
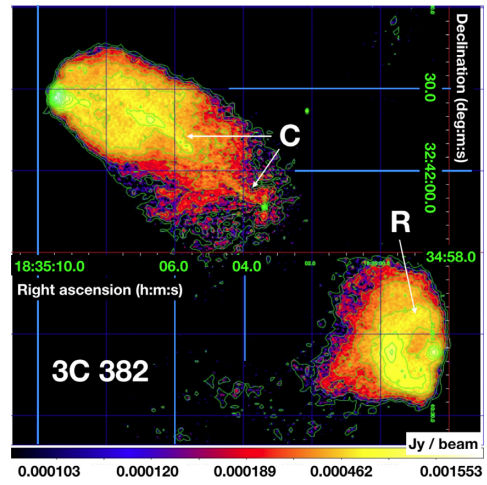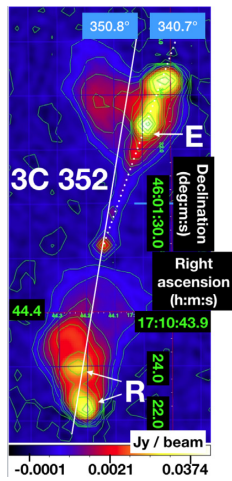

Figure B24. 3C 352, 4.71 GHz, resolution: 0.″35, redshift: 0.37. E: Jets towards edge of lobes; lobe brightness asymmetry on the southern side, R: Multiple hotspots on southern side. Lobe extension on the northern side as expected for precession with long period and wide precession cone (Donohoe & Smith 2016).

Figure B25. 3C 382, 8.47 GHz, resolution: 0.″75, redshift: 0.058. C: Jet bent in northern lobe over whole length, possibly additionally a jet−cloud interaction, R: Ring-shaped southern hotspot. Jet slightly off lobe axis. Crosswind.
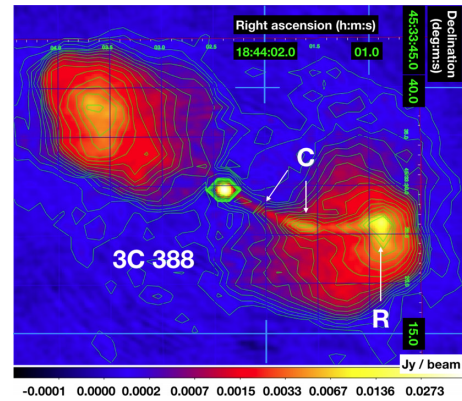
Figure B26. 3C 388, 8.46 GHz, resolution: 0.″783 × 0.″693, redshift: 0.091. C: Obvious curvature in jet. Additionally, bending at bright spot, possibly a jet−cloud interaction. R: Wide western hotspot. Lobe symmetry indicates that jet path would have moved towards the cloud/galaxy recently.
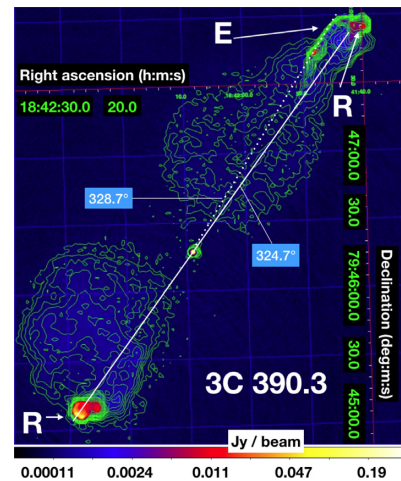

Figure B27. 3C 390.3, 4.99 GHz, resolution: 1″, redshift: 0.057. E: Jet at leeward (see below) edge of lobe, R: Wide terminal hotspots on both sides. Likely crosswind pushing lobes towards east. For the southern lobe, there is an indication for a jet on the western (windward) side of the lobe.
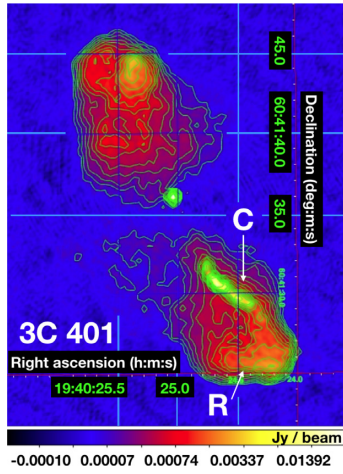
Figure B28. 3C 401, 8.44 GHz, resolution: 0.″27, redshift: 0.20. C: Curved jet on the southern side. E: Jets/hotspots at edge of lobes. Lobe brightness asymmetry on the northern side. R: Wide hotspot/trail of hot back flow on the southern side.
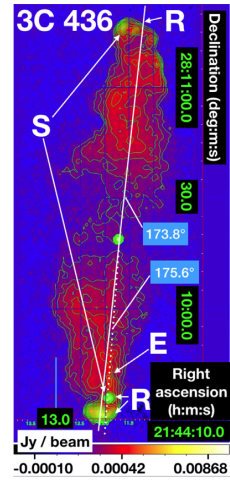

Figure B30. 3C 436, 8.44 GHz, resolution: 0.″75, redshift: 0.21. E: Southern jet at edge of lobe. R: Multiple hotspots. S: Northern hotspots on opposite side of lobe as southern hotspot. Hardcastle et al. (1997) note a jet in the southern lobe, on the western side.
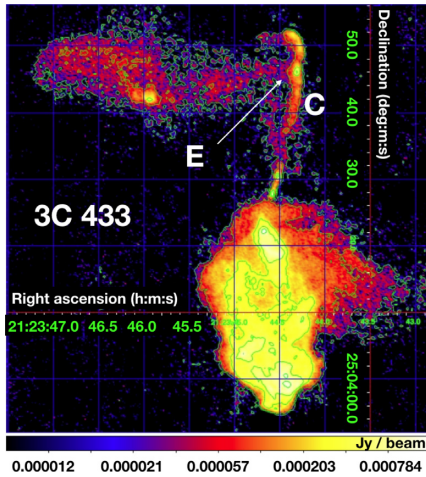

Figure B29. 3C 433, 8.47 GHz, resolution: 0.″25, redshift: 0.10. C: Curved jet on the northern side. E: Misaligned lobe axis on the northern side; lobe brightness asymmetry on the southern side. Additional hotspot in the northeast lobe extension.
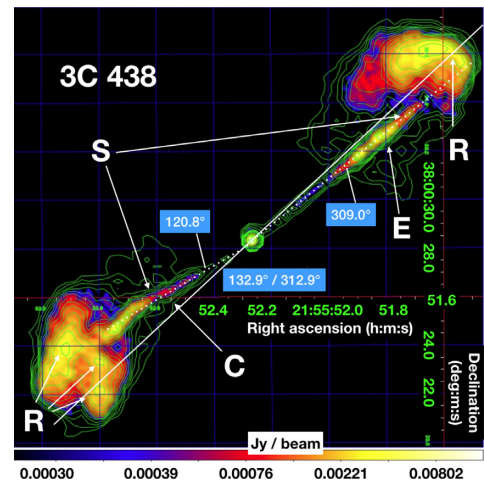

Figure B31. 3C 438, 8.44 GHz, resolution: 0.″23, redshift: 0.29. C: Curved jet on the eastern side. More curvature in counterjet (East). E: Misaligned lobe axis on the western side. R: Wide terminal hotspot on the eastern side. Trail of hot back flow on the western side. S: S symmetric jets. Angle between northern and southern jet $\neq 180°$.
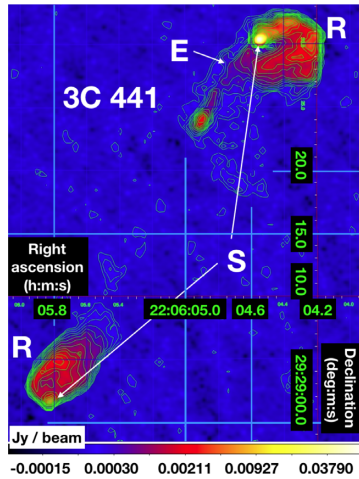
Figure B32. 3C 441, 4.86 GHz, resolution: 0″.35, redshift: 0.71. E: Jet and hotspot at one edge of lobe. R: Wide hotspot/ring-like feature in both lobes. S: Hotspot S-symmetry.
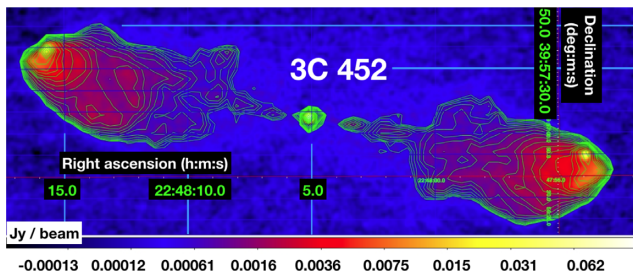

Figure B33. 3C 452, 8.06 GHz, resolution: 2″.1, redshift: 0.081. A cross-wind from north can probably not fully explain the hotspot asymmetry, because a straight line connecting the hotspots would leave the core south. However, since the situation appears doubtful we conservatively assign no precession indicator.

APPENDIX C: NEARBY BINARY BLACK HOLE CANDIDATES

The closest sources are the best candidates for a direct detection of gravitational waves if they indeed contain close binary black holes. We summarize here important data, give an estimate for the precession period and predict the gravitational wave strain (Table 3). We also comment on the presence of a core structure in the stellar profiles where available, which is expected as a result of stars being lost by interaction with the supermassive black hole binary during their mutual approach.

C1 Hydra A

This well-studied radio source has a large-scale S-symmetry (Taylor et al. 1990). An extended 3D simulation study of the jet–environment interaction for this particular source, where source geometry and precession period has been varied, has recently determined the precession period to 1 Myr (Nawaz et al. 2016). This is also compatible with a Gower et al. (1982) model of precessing jets with relativistic aberration (Fig. A1 and Table A1). As argued above for similar precession periods, this precession is most likely related to geodetic precession due to a binary supermassive black hole. The precession period together with the black hole mass of $(5 \pm 4) \times 10^8 \, M_\odot$ (Rafferty et al. 2006) limits the binary separation to a max-

imum of 0.2 pc (equation 2). This is accessible to high-resolution radio imaging. A helical pattern would hence be expected for the parsec-scale jet unless the jet is produced by the primary in a very unequal mass binary. The parsec-scale image shows a straight jet (Taylor 1996). This might mean that in this source the jet is indeed produced by a dominant primary. The parsec-scale jet is obviously misaligned with the large-scale jet, as expected for a precessing source.

C2 Centaurus A

Similar to Hydra A, Cen A is also a source with S-symmetric structure (Fig. C1, Morganti et al. 1999b). The inner structure has a size and geometry very similar to Hydra A, suggesting also a precession with period of approximately 1 Myr. We can also estimate the precession period from the X-ray image (Fig. C1). The bow shock in the ambient gas is clearly detected. Croston et al. (2009) analyse the shock and derive a source age of 2 Myr. The southern bow shock has an extension which could be related to the current impact of the jet. If the precession period was comparable to the source age, the extension would be comparable in size to the overall bow shock region. The fact that a small extension is observed requires that the precession period is significantly less than 2 Myr, consistent with the above estimate. The argument becomes stronger, if even the observed bow shock extension was not related to the current impact of the jet. The jet is straight for about 4.5 kpc (Hardcastle et al. 2007). This requires a precession period significantly longer than 0.02 Myr. We adopt 1 ± 0.5 Myr as an estimate. The faint X-ray counterjet (Hardcastle et al. 2007) appears more strongly curved than the jet, consistent with expectations for relativistic aberration from a precessing jet (Gower et al. 1982). Assuming a binary black hole with a total mass of $(5.5 \pm 1) \times 10^7 \, M_\odot$ (Cappellari et al. 2009), a separation of less than about 0.05 parsec is derived (equation 2). Müller et al. (2014) present high-resolution VLBI images of Cen A with similar resolution. No sign of a secondary radio core is seen. This could indicate that the separation is smaller than 0.05 pc, or that the secondary core was not luminous enough at the time of observation, possibly because the secondary black hole is smaller. The stellar density as a function of radius shows a core structure, as expected for a binary supermassive black hole, and a dust lane signifies a recent galaxy merging event (Marconi et al. 2000).

C3 M87

Low-frequency radio imaging establishes the average direction of a previous outburst to be north–south (Owen, Eilek & Kassim 2000). The current jet direction is towards $PA \approx 300°$. The black hole of mass of $(6.6 \pm 0.4) \times 10^9 \, M_\odot$ (Gebhardt et al. 2011) is unlikely to have accreted a significant fraction of its mass in the last 5×10^7 yr since the last outburst. Hence, accretion has not changed the spin axis. The current jet is traced down to a few Schwarzschild radii and stays straight, hence there is no jet–cloud interaction. The fossil outburst has lasted too long so any clouds that would have affected the past jet would have been ablated too quickly to influence the long-term average symmetry. Hence, the difference between the symmetry axis of the older, large-scale lobes and the current jet direction is significant. A binary black hole could cause this in two ways: the current and previous outbursts could come from different black holes with different spin axes, or the spin axis has precessed to the different current location. In order to change direction between the outbursts, the precession period has to be less than about 10^8 yr. The fact that the jet is straight over about 1 kpc from the core
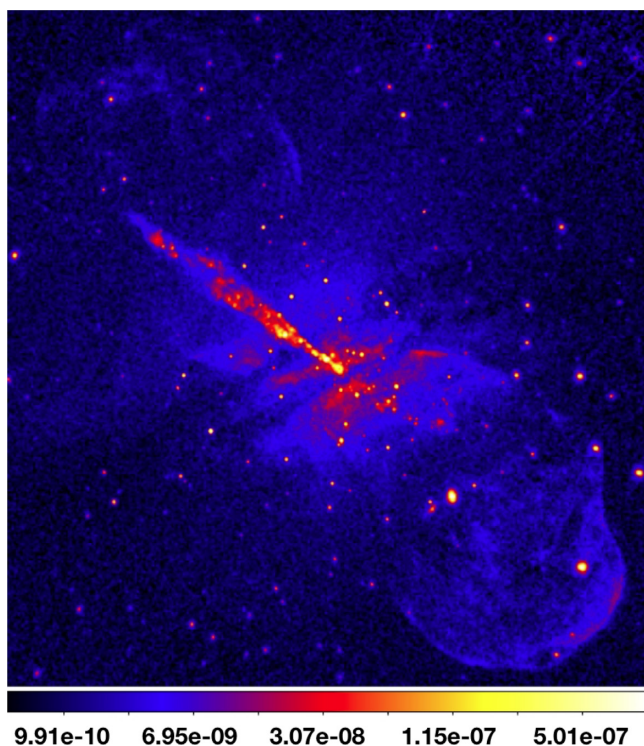
Figure C1. *Chandra* X-ray image of Centaurus A, exposure-corrected image in the 0.4–2.5 keV band taken from the data set presented by Hardcastle et al. (2007). The bright X-ray structure emphasizes the current jet, whereas the extended X-ray emission identifies the long-term average of the jet direction. The extent of this part of the source is about 11 kpc. S-symmetry and a misalignment of the jet with the lobe axis suggest precession. There is a weak indication of a curved counterjet.
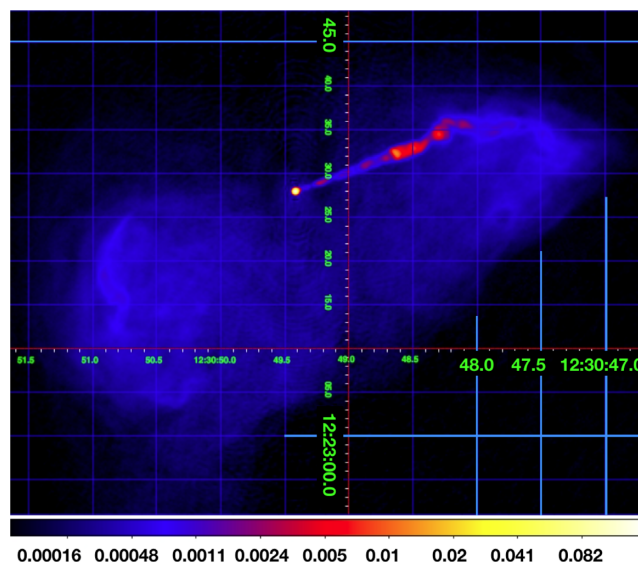

Figure C2. 4.6 GHz image of M87; data from Hines, Owen & Eilek (1989). The jet is at the edge of the radio lobe, an indication of precession.

suggests a period longer than about 10^5 yr. The asymmetry of the current source's radio lobes (Fig. C2) is reminiscent of simulations of precessing jets with source age similar to the precession period (Donohoe & Smith 2016). This suggests that the precession period is indeed comparable to the current source age, about 1 Myr. We conservatively adopt a range of 5 ± 2 Myr as precession period. M87 has a stellar core profile (Côté et al. 2006).

This paper has been typeset from a TEX/LATEX file prepared by the author.